The Tongon Au Deposit, Northern Côte d'Ivoire: An example of Birimian Au Skarn Mineralization

D.M. Lawrence[1*†], A.H. Allibone[1, 2], Z. Chang[3], S. Meffre[4], J.S. Lambert-Smith[5**], P.J. Treloar[5]

[1]Randgold Resources Ltd, Halkett Street, St Helier, Jersey, Channel Islands, JE2 4WJ

[2]Rodinian (NZ) Ltd, PO Box 758, Wanaka 9343, New Zealand

[3]College of Science, Technology & Engineering, James Cook University, Townsville, Queensland, Australia

[4]University of Tasmania, Earth Sciences (Geology, Geophysics & Geochemistry), Hobart, Tasmania, 7001

[5]Deparment of Geography and Geology, Kingston University, Penrhyn Road, Kingston upon Thames, London, United Kingdom, KT1 2EE

† Corresponding author: email, David.Lawrence@randgold.com

***Electronic Appendix Table A1 for this paper can be found at www.economicgeology.org.**

****Present address: School of Earth and Ocean Sciences, Cardiff University, Main Building, Cardiff, Wales CF10 3AT.**

Key words- Birimian, Eburnean Orogeny, Au skarn mineralization, Côte d'Ivoire

Abstract

The Tongon deposit in northern Côte d'Ivoire is the first reported occurrence of Au skarn mineralization hosted in Paleoproterozoic greenstone rocks of the West African craton. Tongon is an unusually large skarn (3.8 Moz at 2.5 g/t Au) replacing noncarbonate host rocks. The deposit is hosted exclusively in basaltic-andesitic crystal tuffs of the Senoufo greenstone belt. All other rock types in the local stratigraphy, including carbonaceous shales, siltstones, and dacitic crystal and lapilli tuffs, are devoid of mineralization. This observation implies a strong bulk compositional control on the distribution of the skarn. At the district scale, the Tongon hydrothermal system is confined to a corridor of ENE-striking orogen-oblique transfer faults, which link orogen-parallel N- to NNE-striking reverse faults to the north and south. Ferroan A-type granites and lamprophyric dikes also occur along these orogen-oblique faults. To date, no Au skarn mineralization has been discovered outside the corridor of ENE-striking faults elsewhere in the Senoufo belt.

The alteration haloes surrounding the deposit formed during three main stages: stage 1, early/distal potassic (biotite-K-feldspar-actinolite) metasomatism; stage 2, prograde clinopyroxene ± grossularitic garnet skarn; and stage 3, retrograde skarn consisting of epidote-clinozoisite-prehnite-albite and slightly later quartz-sulfide-Au. Garnets contain high Al and Ti, and the skarns have elevated Ni and Cr, reflecting the mafic composition of the host rocks. Proximal to peripheral mineral zonation patterns are defined by decreases in the ratio of garnet to pyroxene, increasing Fe in pyroxene, higher Au concentrations, and an increase in the intensity of retrograde alteration, seen as a change from white- to green-colored skarn. Spatially, gold-rich stage 3 alteration coincides with stage 2 intermediate diopside-rich skarn and distal hedenbergite-ferroactinolite skarn, whereas the proximal garnet-bearing skarn typically has much lower Au grades.

Fluid inclusions studies in the prograde skarn assemblages show primary, high temperature (>400°C), moderately saline (8–14 wt % NaCl equiv) H_2O-NaCl-$CaCl_2$ inclusions, with pressures estimated at 2 ± 0.5 kbar. The source of these fluids remains unclear, as plutonic rocks immediately to the west of Tongon intrude the skarn. U-Pb dating of hydrothermal titanite indicates the Au skarn formed between 2139 ± 21 and 2128 ± 21 Ma, 20 to 70 m.y. before the major episode of orogenic Au mineralization in southwest Ghana and western Mali. Dating provides further evidence that Au mineralization within the Paleoproterozoic rocks of West Africa craton occurred over several tens of millions of years through a variety of different processes.

Introduction

Gold, rather than base metals, is the principal metal in a small subset of mineralized skarns commonly referred to as Au skarns (Meinert, 1998). The term "skarn" is used here to describe calc-silicate metasomatism of any rock type, not just alteration confined to carbonate rocks (Meinert, 1998; Meinert et al., 2005). Phanerozoic Au skarns are generally associated with replacement of carbonate host rocks located proximal to weakly reduced hypabyssal (<5 km) intrusive source rocks (Meinert, 1998, 2000; Meinert et al., 2005). Rare occurrences of structurally controlled Au skarn have also been recorded from deeper crustal levels (5–10 km) in Precambrian metamorphic terranes. These orebodies are hosted in volcanic and siliciclastic rocks where primary carbonates are minor or rare (e.g., Pan et al., 1991; Mueller, 1997; Mueller et al., 2004). The geologic relationships between skarn and Au mineralization in these deeper Au deposits are uncertain, and the relative importance of magmatic, metamorphic, and mantle-derived fluids in their origin commonly remains unclear (Meinert, 1998).

This paper describes the ca. 4 Moz, ~2.5 g/t Au grade (mined and in situ mineral resources) Tongon deposit in northern Côte d'Ivoire, which consists of two open cut pits referred to as Tongon South and Tongon North. Tongon represents one of the first major Au skarn deposits recognized in the well-endowed Paleoproterozoic (Birimian) rocks of the West African craton and one of the largest Au skarn deposits discovered to date globally. The Tongon Au skarn provides the opportunity to study the origin of Au skarn-forming fluids in Paleoproterozoic greenstone belts and the structural setting(s) likely to be prospective for similar deposits. The data reported in this paper also highlight the diversity of Au deposits in the Paleoproterozoic rocks of West Africa, many of which have only been recognized in the last ca. 10 years (e.g., McFarlane et al., 2011; Lawrence et al., 2013a, 2016; Treloar et al., 2014; Hein et al., 2015; Béziat et al., 2016; Masurel et al., 2016; Le Mignot et al., 2017).

Regional Geology

Tongon is situated in the northern part of the southern West African craton, along the ca. 30-km-wide Paleoproterozoic (Birimian) Senoufo greenstone belt (inset, Fig. 1). The Senoufo belt strikes north-northeast to northeast and extends into western Burkina Faso where it hosts the Nogbele, Fourkoura, Samavogo, and Stinger group of Au deposits (Brooks and Cameron, 2009). The belt is flanked to the east and west by granite-gneiss terranes of unknown age. Neighboring volcano-sedimentary belts include the Fetekro belt 120 km to the southeast (Doumbia et al., 1998) and the Boundiali belt 80 km to the west, with the Syama Au deposit located on its western margin (Olson et al., 1992; Ballo et al., 2016).

Senoufo geology

The geology of the Senoufo belt is illustrated in Figure 1. Supracrustal rocks within the belt include basaltic to andesitic ash and lapilli tuffs, pyroclastic breccias, tholeiitic basalts and minor andesites, carbonaceous shales, shales, and siltstones. Basaltic lavas form an increasingly large proportion of the Senoufo belt toward the northeast. Intermediate to basic volcanic and volcaniclastic rocks are typically overprinted by greenschist facies, regional metamorphic assemblages. More intensely deformed amphibolite facies mafic schists are present on the eastern margin of the belt toward its northern end (Fig. 1). Several major granitoid plutons intrude supracrustal rocks of the Senoufo belt (Fig. 1). Older, weakly foliated plutons include ferroan A-type granites (e.g., Nafoun granite) and have geometries which are concordant with the structural grain of the belt. Younger, discordant plutons include hornblende-bearing granodiorites and diorites and late-kinematic potassic granites.

Senoufo structure

Rocks of the Senoufo belt were deformed and metamorphosed during the Eburnean orogeny between 2.2 and 2.1 Ga (Abouchami et al., 1990; Allibone et al., 2002a, b; Hein, 2010; Perrouty et al., 2012; Baratoux et al., 2015). A N- to NE-striking structural grain, defined by the strike of stratigraphic units and major faults, is the most obvious kilometer-scale structural feature within the Senoufo belt (Fig. 1). In those areas where outcrop and/or drill core are available, obvious penetrative foliation(s) are confined to discrete faults, shear zones, and their immediately adjacent rocks. Most rocks in the Senoufo belt remain unfoliated. Amphibolite facies schistose rocks with a penetrative foliation are confined to the eastern side of the belt, north of Tongon.

The profile of geophysical anomalies associated with stratigraphic units in images of the magnetic and electromagnetic (EM) data imply that bedding generally dips >60° to the northwest, an inference confirmed by limited outcrop measurements in the northern part of the belt. Volcaniclastic units in the vicinity of the Tongon South deposit dip 30° to 50° toward the northwest, but this relatively gentle dip appears to be a local feature. Graded bedding in sandstones and siltstones at the Djinni prospect west of Tongon (Fig. 1) indicates younging of the stratigraphy toward the southeast, whereas volcaniclastic units on the northern side of Tongon North young toward the northwest. This change in stratigraphic younging direction, when coupled with the steep dip of bedding, implies the presence of km-scale, tight to isoclinal upright folds within the belt.

The positions of several >50-km-long, N- to NE-striking Eburnean faults have been inferred from breaks in the continuity of EM anomalies where these faults locally cut across bedding at small angles. These inferences are supported by rare drill hole intersections of carbonaceous phyllite, strongly foliated sericite ± carbonate-altered shear zones, and narrower bands of late cataclasite that cut the foliated fault rocks. No outcrop-scale indicators of the sense or direction of shear were observed

within these faults. However, rotation of bedding into a steeply dipping orientation throughout most of the ca. 30-km width of the belt may have occurred along major curved reverse faults during a period of region-wide contractional deformation (e.g., Twiss and Moores, 1992), suggesting movement on the faults was largely reverse rather than strikeslip or normal. The lack of higher grade metamorphic rocks throughout most of the Senoufo belt could be explained by soling out of these faults along a midcrustal detachment above the greenschist-amphibolite facies transition.

A ca. 2-km-wide zone of E- to ENE-striking faults cuts across the Senoufo belt in the vicinity of the Tongon Au deposits (Fig. 1). These faults link N- to NE-striking faults to the north and south. Bedding also swings into an E- to ENE-striking orientation in the vicinity of these faults. At Sekala one of these east-striking faults comprises a 150-m-wide zone of strongly foliated sericite-carbonate–altered rock that contains numerous centimeter- to meter-scale intrashear folds and variably deformed quartz-carbonate veins. The E- to ENE-striking fault in the immediate footwall of the Tongon North deposit composes a ca. 20-m-wide zone of carbonaceous schist that dips 70° to 85°N. The E- to ENE-striking faults appear to be restricted to the area around Tongon. No other major faults with this orientation occur in the Senoufo belt (Fig. 1). The Tongon Au deposits and adjacent Tongon granodiorite are located in a km-scale sinistral jog in the zone of E- to ENE-striking faults where the number and spacing of the faults change.

Methodology

Geologic maps and cross sections for this study are largely based on mapping of the Tongon open pits and logging of drill core and drill chips, as intense laterization has destroyed most outcrop throughout the Tongon area. Airborne magnetic and electromagnetic data were also used to help identify and constrain the extent and orientation of stratigraphic units, granitoid plutons, and faults. Deposit-scale studies were largely concentrated on the main orebodies at Tongon South and Tongon North, although nearby prospects were also investigated. Approximately 100 representative samples were examined using optical and scanning electron microscopy and microprobed at Kingston University London. The electron microprobe operating parameters are the same as those reported in Lawrence et al. (2013a).

Whole-rock geochemical analyses of unaltered and altered Tongon rocks were carried out by Cardiff University. Approximately 0.5 to 1 kg of fresh and homogeneous rock was collected per sample, with weathered surfaces removed prior to crushing and milling. Samples were made into lithium metaborate fusion beads and then dissolved and analysed by inductively coupled plasma-optical emission spectrometry (ICP-OES) and inductively coupled plasma-mass spectrometry (ICP-MS), using a JY Horiba Ultima2 system and a Thermo Elemental X series (X7) system, respectively. International

standards (JB1a, JG1a, NIM-G) were used to monitor data quality. Based on the comparison with accepted values for the standards, the accuracy of the data was typically within a 2% error for the major elements and generally within a 5% error for trace elements. Precision levels were generally better than 5%.

U-Pb geochronological analyses were carried out on titanites from two skarn samples and on zircons from three samples of the crosscutting Tongon granodiorite in order to constrain the timings of deformation, magmatic, and mineralization events in the Tongon district. Laser ablation-inductively coupled plasma-mass spectrometry (LA-ICP-MS) U-Pb dating (Jackson et al., 2004; Chang et al., 2006) was undertaken at the University of Tasmania using the methods detailed in Yang et al. (2015), with the following modifications for titanite analyses. Downhole fractionation, instrument drift, and mass bias correction factors for Pb/U in titanite were calculated using an in-house primary titanite standard 100606 (Best, 2012) and secondary zircon standards Mt Dromadery (Schoene et al., 2006) and FC-3 (Schmitz and Bowring, 2001). These were performed at the beginning of the session and after every 12 unknown titanite spots. The correction factor for the $^{207}Pb/^{206}Pb$ in both zircons and titanites was calculated from analyses of NIST610 every 30 unknowns and corrected according to Baker et al. (2004). Isotopes measured during analysis of titanites were ^{49}Ti, ^{56}Fe, ^{43}Ca, ^{140}Ce, ^{202}Hg, ^{204}Pb, ^{206}Pb, ^{207}Pb, ^{208}Pb, ^{232}Th, and ^{238}U. Titanite data reduction used the method of Halpin et al. (2014). Common Pb in the primary standard was corrected for after the method of Chew et al. (2011).

Twenty-five samples from Tongon South and Tongon North were selected for fluid inclusion analysis and prepared as doubly polished wafers approximately 100 µm in thickness. Microthermometric studies were carried out at Kingston University London using a Linkam THMSG600 stage with a Nikon Optiphot microscope. The stage was regularly calibrated using a Linkam synthetic H_2O-CO_2 standard. A heating rate of 1°C min-1 was employed close to phase change (precision of approximately ±0.2°C). Calculations of pressure-volume-temperature-composition (PVTX) properties of fluid inclusions, based on the microthermometric data, were made using the software package FLUIDS (Bakker, 2003). The equations of state used were Zhang and Frantz (1987) for bulk fluid properties and densities and Bodnar and Vityk (1994) and Knight and Bodnar (1989) for the construction of isochores.

Sulfides from mineralized rock were also analyzed for sulfur isotope compositions ($\delta^{34}S$). Approximately 5 mg of sulphides were separated by crushing, sieving, and handpicking down to 250 µm. The purity of each sulfide sample was greater than 90%. Analysis was carried out at the Scottish Universities Environmental Research Centre (SUERC) at East Kilbride in Scotland, using standard techniques (Robinson and Kusakabe, 1975). Lab reproducibility (1σ) for $\delta^{34}S$ is ±0.2‰. Data are reported in standard notation as per mil (‰) variations from the Vienna Cañon Diablo Troilite (V-CDT) international standard.

Deposit Geology

Tongon South

Although the Tongon South deposit is situated within the zone of ENE-striking faults at the district scale (Fig. 1), mineralization occurs in and around several closely spaced, parallel, N and NNE-striking brittle faults that dip 30° to 50° to the west and west-northwest in the southern part of the deposit and ~70° to the west-northwest in the northern part (Figs. 2, 3A). These faults extend >2 km along strike but terminate downdip where they are cut by the younger Tongon granodiorite (Fig. 2). Replacement breccias resulting from varying degrees of skarn alteration of the host rocks occur in the damage zone that surrounds these deposit-scale faults (Fig. 3B-C).

The stratigraphy at Tongon South consists of a >400-m-thick package of metamorphosed basaltic-andesitic crystal tuffs that dips 30° to 50° to the northwest, parallel to the aforementioned brittle faults (Figs. 2, 4A). The whole-rock geochemistry of this rock type is presented in Table 1. The tuffs include subrounded, well-sorted fragments of augite and hornblende and feldspar laths 400 to 1,000 μm in size in a matrix predominately of devitrified glassy material (Fig. 4B). Crystal matrix ratios are approximately 60:40. Layers of coarser polymict lithic volcanicaniclastic rocks 10 to 25 m thick are interbedded within the basaltic-andesitic crystal tuffs. These coarser volcaniclastic rocks contain fragments of porphyritic granitic rocks, bedded siltstone and carbonaceous shale, and aplite and ultramafic rocks (Fig. 4C-D). Unaltered, fine-grained carbonaceous shales, shales, and siltstones occur 150 to 200 m below the deposit (Fig. 2). No limestone units occur in the stratigraphy at Tongon.

The Tongon granodiorite, with a surface extent of approximately 7 to 8 km^2, cuts the western margin of the deposit and is unaffected by skarn and mineralization. Smaller dikes and apophyses of the Tongon granodiorite 3 to 15 m thick cut the mineralized skarns east of the main contact (Fig. 2). Wholerock geochemical data from the granodiorite are presented in Table 1. The pluton is largely undeformed, medium-grained (1–3 mm), and equigranular (Fig. 4G). It comprises 45 to 50% partially altered andesine, ~10% microcline, 20 to 25% quartz, 10 to 15% hornblende, and 5 to 10% biotite, with magnetite the dominant opaque mineral (Fig. 4H). Amphiboles and biotite show Mg-rich compositions with mean X_{Mg} of 0.72 and 0.57, respectively (App. Table A1). The Al_2O_3 content of hornblende ranges from 6.21 to 7.39 wt %, implying pressures of 2 ± 0.5 kbar at the time of crystallization using the Hammarstrom and Zen (1986) geobarometer. Mafic enclaves are common throughout that part of the pluton exposed in the Tongon South open pit. The extent of the contact aureole surrounding the Tongon granodiorite is not well constrained; however, a narrow zone (<20 m) of hornblende hornfels is observed in unaltered basaltic-andesitic tuff in the Tongon South pit. Other minor intrusive rocks that cut the orebody include K-rich granite dikes <5 m wide, lamprophyres,

dolerites, and porphyritic diorites. The ultramafic-mafic, intermediate dikes are more abundant and continuous at Tongon North and thus are discussed in further detail below. Late NNE- and NNW-striking, narrow, sericite- and chlorite-altered faults and fractures crosscut the Tongon granodiorite and adjacent skarns. Both steep and gently plunging slickenlines are present along the fault surfaces, indicating that at least two phases of movement occurred on these faults. These late faults and their associated alteration locally contain minor amounts of pyrite and sub g/t Au, indicating that they were active during a later, weaker mineralizing event, after skarn formation and emplacement of the Tongon granodiorite.

Tongon North

The Tongon North deposit is located in the immediate hanging wall of one of the main ENE-striking faults in the region, 1 km to the north-northeast of Tongon South (Fig. 5). The orebody consists of a single fault-bounded lode 2.2 km long and 3 to 40 m wide with an average width of 10 m. The fault is marked by a ca. 20-m-wide zone of deformed carbonaceous shale that dips 65° to 80° north-northwest. Altered and mineralized rocks adjacent to the carbonaceous shale are also deformed, indicating that movement on the ENE-striking fault continued after skarn development and associated Au mineralization. Although replacement breccias are less prominent than at Tongon South, fluid flow at Tongon North also appears to have been focused through a planar zone of pervasive fracturing.

The volcano-sedimentary rocks in the vicinity of Tongon North strike 60° to 80° and dip 65° to 80° north. Mineralization is hosted by a 10- to 50-m-thick layer of basaltic-andesitic crystal tuffs, similar to those at Tongon South (Figs. 4A-B, 5). This unit is structurally overlain by minor carbonaceous shales, siltstones, and a >200-m-thick package of dacitic crystal and lapilli tuffs that are unaltered (Fig. 4E). The dacitic tuffs include both lithic and welded varieties. The lithic tuffscontain lapilli particles 2 to 4 mm in size and 200-µm- to 2-mm-long crystals of plagioclase in a matrix of plagioclase, quartz, prismatic amphibole, and minor biotite. The fragment- matrix ratio is approximately 30:70. The welded tuffs are slightly coarser and more poorly sorted. They contain flattened and aligned lapilli particles 2 to 6 mm in size, finer crystals of plagioclase, subrounded quartz, and minor 400-µm- to 2-mm pyroxene grains (Fig. 4F). The footwall of the Tongon North deposit is comprised of deformed carbonaceous shale units 5 to 20 m thick interbedded with basaltic-andesitic crystal tuffs (Fig. 5).

The Tongon granodiorite cuts the hanging wall of the western part of the Tongon North deposit and is itself cut by medium-grained, lamprophyre dikes 2 to 7 m thick. (Figs. 4I-J,5). The least-altered lamprophyre dikes consist of 30 to 35% primary biotite, 25 to 30% orthoclase, 10 to 20% diopside, 5 to 10% plagioclase, 5 to 10% amphibole, 1 to 5% melilite, and 2% Ti-rich magnetite. Phenocrysts include biotite, lesser pargasite, diopside, and rare melilite. Feldspar is restricted to the groundmass

with plagioclase/alkali feldspar ratios of approximately 1:3. Ocelli textures are common in the lamprophyres with cavities up to 6 mm in size filled with secondary quartz (Fig. 4I). Older dikes at Tongon North include finegrained dolerite, undifferentiated mafic dikes, and plagioclase-hornblende-biotite phyric diorites emplaced before or during skarn development. The undifferentiated mafic dikes are largely confined to the southern side of the ENE-striking fault, which marks the footwall of the deposit. They consist of a mixture of strongly deformed intrusive rocks, some of which are probably early lamprophyres.

The Tongon Hydrothermal System

The Tongon South and Tongon North deposits have complex but similar mineral paragenesis that includes three main alteration stages: stage 1, biotite ± K-feldspar; stage 2, prograde skarn assemblage of pyroxene-garnet; and stage 3, retrograde skarn including prehnite-clinozoisite-epidote-albite-pumpellyite-calcite and quartz-sulfide-Au (Figs. 6, 7). A later minor stage (stage 4) of chlorite-sericite ± quartz ± minor pyrite ± Au alteration is also observed. Stages 1 to 3 are exclusively confined to basaltic-andesitic tuffs and are absent from carbonaceous shales and dacitic tuffs in the immediate footwall and hanging wall of the Tongon North deposit (Fig. 5). Each of these four alteration stages is discussed separately below. Whole-rock geochemical analysis of altered rocks and mineral chemical data (SEM-EDS) for the various alteration stages are presented in Table 1 and electronic Appendix Table A1, respectively.

Stage 1: Biotite ± K-feldspar alteration

Early potassic metasomatism of the basaltic-andesitic tuff host rocks (Fig. 6A) typically represents approximately 3 to 10 vol % of the skarn-altered rocks affected by stages 2 and 3, and locally up to 30 vol %. The outer limit of this alteration halo is unclear, although it appears to extend farther into the footwall than later overprinting alteration stages at both orebodies (Figs. 2, 5). Stage 1 assemblages contain finegrained (20–50 µm), euhedral to subhedral biotite and lesser amounts of K-feldspar and minor actinolite and ilmenite. Biotite replaced primary augite and hornblende and locally formsaggregates (200–300 µm in diameter) surrounded by coronas of fine-grained plagioclase and amphibole. Hydrothermal biotite is more aluminous and magnesian (XMg = 0.66) than magmatic biotite (X_{Mg} = 0.57) in the neighboring Tongon granodiorite (Table A1). Altered rocks at both orebodies have 0.27 to 2.59 wt % K_2O (Table 1), with significant mass gains in K_2O and Rb compared to unaltered basaltic-andesitic tuffs (Fig. 8).

Stage 2: Prograde pyroxene ± garnet alteration

The stage 2 prograde skarn is the most intensely developed and widespread hydrothermal assemblage at both Tongon South and Tongon North. It typically replaces 30 to 70% of primary and stage 1

minerals. The protolith of the more massive skarns was identified by whole-rock geochemical analysis or by tracing bedding planes up dip to where the skarn replacement was less intense. Skarn samples show similar concentrations of high field strength elements (HFSE), Ti (TiO_2 = 0.6–0.8 wt %), Ti/Y ratios (200–300), V (170–230 ppm), Co (40–50 ppm), Sc (25–40 ppm), and Zr (61–82 ppm) contents to unaltered basaltic-andesitic tuffs (Table 1). Haloes of pyroxene ± garnet alteration 10 to 80 m wide occur around the damage zone surrounding the aforementioned mineralized faults (Figs. 2, 5). Replacement breccia textures are dominant along narrow fracture networks. (Fig. 6A-E). Variations in the relative amounts and composition of clinopyroxene and garnet define three mineralogically distinct zones (termed zones A-C) within the stage 2 mineral assemblages (Fig. 9; Table 2).

Zone A occurs along the western side of both orebodies (Figs. 2, 5), and skarn has pyroxene-garnet ratios of 5:1 to 15:1. Garnet occurs as coarse poikiloblasts up to 2 cm across in zones of massive clinopyroxene alteration (Fig. 6B) and stockwork veins 0.5 to 5 cm thick surrounded by selvages of clinopyroxene alteration (Fig. 6C-D). Garnets generallyhave grossular-rich compositions with subordinate andradite ($Gr_{30–85}Ad_{5–69}Sp_{0–6}Alm_{0–6}$; mean of $Gr_{61}Ad_{35}Sp_1Alm_3$) (Fig. 9A; Table A1). More andradite-rich garnet is seen in the northern parts of Tongon South. Pyroxenes have diopsidic compositions ($Di_{48–71}Hd_{27–51}Jo_{0–5}$) (Fig. 9B; Table A1). Minor stage 2 minerals present in zone A include, in decreasing order of abundance, andesine, actinolite, fluorapatite, fluorite, titanite, and allanite. These minerals occur as inclusions in garnet and pyroxene or as intergrowths on the margins of garnet and pyroxene. Trace opaque minerals include chromite, pyrrhotite, chalcopyrite, bornite, pentlandite, and sphalerite.

Garnet decreases in abundance eastward in both orebodies with zone B assemblages dominated by modestly diopsidic pyroxene ($Di_{54–82}Hd_{18–44}Jo_{0–5}$; mean of $Di_{68}Hd_{30}Jo_2$) (Fig. 9B; Table A1). Locally within zone B, diopside-dominated pyroxene (mean of $Di_{90}Hd_9Jo_1$) is accompanied by forsterite, phologopite, and tremolite in thin, <1-m beds of altered basaltic tuff. Zone B assemblages grade eastward and outward into Fe-rich zone C assemblages that are dominated by more hedenbergite-rich clinopyroxene ($Di_{26–64}Hd_{34–73}Jo_{0–6}$; mean of $Di_{45}Hd_{54}Jo_2$) (Fig. 9B; Table A1) and ferro-actinolite (Fig. 6A). Less common minerals in zone C assemblages include wollastonite and minor andradite (mean $Gr_{27}Ad_{70}Sp_2Alm_1$) (Fig. 9A; Table A1), with traces of quartz, apatite, chalcopyrite, and titanite.

The intensity of stage 2 alteration is highest in zone A and decreases to the east in both orebodies. Isocon mass balance plots (after Grant, 1986), displaying the whole rock compositional changes during skarn alteration (Fig. 8), indicate an overall net mass gain of 28% in zone A and a 10 to 15% mass gain in zones B and C. In addition to increases in K_2O and Rb largely caused by stage 1 alteration, skarn-altered rocks also show significant increases in CaO (80–180%), MnO (70–170%), LOI (H_2O; 216–553%), and Cu (49–99%) in all zones compared to unaltered footwall basaltic-andesitic tuffs (Fig. 8). Zones A

and B also show mass gains in MgO (10–15%), Cr (77–103%), and Ni, (70%); whereas zone C shows minor increases in total Fe expressed as Fe_2O_3 (9%).

Stage 3: Retrograde calc-silicate-albite-carbonate-quartz alteration

Prehnite-epidote-calcite-clinozoisite-albite-pumpellyite: Stage 2 garnet and clinopyroxene are partly replaced by finer-grained stage 3 calcite, epidote, clinozoisite, prehnite, pumpellyite, actinolite, and albite assemblages (Fig. 10). Epidote, clinozoisite, prehnite, albite, and calcite replace grossular garnet and diopsidic pyroxene (Fig. 10A-C) in zones A and B, whereas prehnite, pumpellyite, and albite partially replace hedenbergitic pyroxene and ferro-actinolite in zone C of both deposits (Fig. 10D; Table 2). Prehnite veinlets up to 3 mm thick occur locally within rocks overprinted by stage 3 assemblages. The narrow zones of Mg-rich prograde skarn (stage 2 diopside, phlogopite, tremolite, and forsterite) are partly replaced by talc, serpentine, calcite, magnetite, and anhydrite during stage 3 alteration. Stage 3 alteration is most intense in the central and eastern parts of both deposits in rocks previously overprinted by stage 2 zone B and C assemblages.

Quartz-sulfide-Au: The main phase of Au mineralization at Tongon is temporally and spatially associated with stage 3quartz, sulfide ± minor ankerite alteration, which occurs as alteration haloes 5 to 40 m wide around the mineralized faults (Figs. 2, 5). This phase of alteration overprints the stage 2 skarn assemblages (Fig. 6F) and occurred during or after prehniteepidote-calcite-clinozoisite-albite-pumpellyite alteration. The intensity of quartz alteration varies from weakly diffusive zones (Fig. 6F) to more intense texture-destructive zones of multiphase alteration (Fig. 6G). At Tongon South, stronger zones of silicification are localized at bends and intersections in the network of brittle faults. At Tongon North, more intense silicification forms a single, approximately planar zone in which increases in alteration intensity correlate with increases in Au grade. Samples of strongly silicified rock were not included in the whole-rock geochemical study (Table 1; Fig. 8).

Gold is associated with disseminated and stringer veinlets of pyrrhotite (~45%), arsenopyrite (~25–30%), pyrite (~20–25%), and löllingite (1–5%). Mineral textures suggest that sulphides crystallized in the following order (Figs. 7, 11):

löllingite + pyrrhotite → arsenopyrite + pyrite → late pyrrhotite + minor chalcopyrite.

Löllingite and pyrrhotite-I grains are generally <200 μm in size and have reacted to form arsenopyrite rims around löllingite (Fig. 11A-B). Arsenopyrite also occurs as aggregates of subhedral, rhombic, and acicular grains commonly intergrown with pyrite (Fig. 11C). Minor and trace sulfides associated with arsenopyrite and pyrite include sphalerite, cobaltite, gersdorffite, and bismuthinite; the latter is associated with Au alongthe eastern side of Tongon North. Late pyrrhotite-II forms aggregates of

grains up to 3 mm across, selectively replaces pyrite along microfractures, and rims arsenopyrite and pyrite (Fig. 11A, D). Chalcopyrite typically occurs as inclusions in pyrrhotite-II.

Arsenopyrite and löllingite are the main sulfides associated with gold, with a strong Au-As correlation measured in both orebodies (r = 0.67; Fig. 12). Approximately 75% of the Au particles are 5 to 20 µm across (Fig. 11E), with less common, coarser particles up to 250 µm in diameter. Less than 5% of the Au occurs as nanoparticles <0.3 µm in size. Microprobe analysis of the native Au grains indicate an average fineness of 900, although electrum with up to 55 wt % Ag is locally present. Arsenic levels in arsenopyrite (mean of 34.1 at. % ± 1.1%) (Table A1) imply that stage 3 quartz-sulfide-Au mineralization formed at a temperature of ~400° to 470°C, using the Sharp et al. (1985) modification of the Kretschmar and Scott (1976) geothermometer.

Stage 4: Minor late chlorite-sericite ± quartz ± minor Au

Discontinuous zones of postskarn stage 4 alteration are localized along the late north-, NNE-, and NNW-striking faults and fractures within the Tongon granodiorite and surrounding rocks (Fig. 6H). Alteration in the granodiorite includes sericitization of K-feldspar and plagioclase and chloritization and hematite staining of hornblende and biotite. A fine network of pale-green sericite-carbonate-quartz veins and chlorite veinlets are also associated with stage 4 alteration. Minor disseminated pyrite, arsenopyrite, and anomalous low-grade Au (<1 g/t) are associated with chlorite-sericite alteration. This style of alteration is more widespread outside of the corridor of ENE-striking faults that host the Tongon deposit and is the main phase of Au mineralization in the Seydou South, Seydou North and Jubula prospects northeast of Tongon (Fig. 1).

Geochronology

Titanite from the Tongon South skarn and zircons from the Tongon granodiorite have been dated using LA-ICP-MS U-Pb methods. The results are illustrated on Tera-Wasserberg plots in Figure 13. The spot analyses of the zircon samples were mostly concordant, although a few discordant ages interpreted to result from Pb loss were recorded but not used in calculating the final $^{206}Pb/^{207}Pb$ age. For each sample, the youngest group of spot analyses, including a minimum of three concordant spots and with a mean square of weighted deviates (MSWD) less than 1.8 (the largest MSWD of the secondary standards), were used to calculate a weighted average $^{206}Pb/^{207}Pb$ age. The weighted average ages of the zircons all have <1% analytical uncertainty at 95% confidence level. However we report errors at 1% because (1) the accuracy of U/Pb age dating by LA-ICP-MS has been shown to be problematic below 1% errors especially for zircons with particularly low and high U contents (Black et al., 2004; Allen and Campbell, 2012), and (2) comparison of results from different laboratories have shown reproducibility between labs to be 1 to 3% (Klötzli et al., 2009). Regarding the two titanite samples,

individual analyses generally show a linear trend, indicating common Pb involvement. Therefore the U-Pb discordia method was used to calculate the intercept age, with the discordia intersection at the Y axis ($^{207}Pb/^{206}Pb$) fixed at the common Pb value of the Stacey-Kramers single-stage Pb isotope growth model (Stacey and Kramers, 1975). Similarly, the intercept ages had <1% uncertainty but we report 1% uncertainty.

Two samples were dated from the stage 2 skarn at Tongon South. These samples were the least affected by stage 3 alteration. Hydrothermal titanites in both samples occur as undeformed elongate rhombic and bladed inclusions in pyroxene (100–320 µm in size). Sample DLTN005 is from zone A and is dated at 2128 ± 21 Ma (Fig. 13A), whereas SZ06 from zone B gave a statistically similar age of 2139 21 Ma (Fig. 13B).

Three zircon samples were collected from the Tongon granodiorite. Samples DLTN023 and DLTN029 from Tongon South are dated at 2139 ± 21 Ma (Fig. 13C) and 2128 ± 21 Ma (Fig. 13D), respectively. DLTN038 from Tongon North is dated at 2127 ± 21 Ma (Fig. 13E). All three granodiorite samples have statistically identical ages, and similar ages to the hydrothermal titanites, implying skarn mineralization and emplacement of the Tongon granodiorite occurred between ~2160 and 2106 Ma. Although the events were not distinguishable using the dating method, field relationships clearly show that the Tongon granodiorite postdates the skarns at both orebodies (Figs. 2, 5).

Fluid Characteristics

Fluid inclusions

A preliminary fluid inclusion study was carried out to ascertain the characteristics of fluids responsible for prograde and retrograde skarn. All fluid inclusions observed consist of a single, liquid-rich (average degree of fill of 0.85), H_2O-salt type. No evidence of CO_2 was observed during this study.

Fluid inclusions in stage 2 poikiloblastic garnet crystals and coexisting pyroxene are typically 10 to 30 µm in size, irregularly shaped, and occur as isolated inclusions or in small clusters (Fig. 14A). Rare inclusions have negative crystal shapes. Microthermometric data revealed that two populations of inclusions occur in stage 2 garnet and pyroxene. One population has salinities of 8 to 14.3 wt % NaCl equiv and homogenization/decrepitation temperatures between 295° and 419°C. The second, more abundant population has lower salinity from 0.4 to 5 wt % NaCl equiv and homogenization temperatures between 150° and 315°C (Fig. 14B-D). The former group occurs as isolated primary inclusions in the core of garnet crystals, whereas the latter group generally occurs in closer proximity to zones of prehnite, epidote, and clinozoisite replacement in both garnet and pyroxene. Calculated fluid densities range from 0.665 to 0.933 gcm^{-3}. The three reliable eutectic melting temperatures (Te)

obtained for stage 2 inclusions range from –56.2° to –49.1°C, suggesting a mixture of NaCl and $CaCl_2$ (see Davis et al., 1990).

Fluid inclusions in stage 3 Au-bearing quartz alteration samples are generally <20 μm across, subrounded, and occur in diffuse clusters and pseudosecondary trails. All available quartz samples have recrystallization textures such as triple point and polycrystalline textures. Homogenization temperatures and salinities show a wide range, between 130° to 390°C (mean of 198°C; *n* = 82) and 0.4 to 12.5 wt % NaCl equiv (mean of 4.8 wt % NaCl equiv; *n* = 82), respectively (Fig. 14BD). Calculated fluid densities range from 0.514 to 0.991 gcm^{-3} with a mean of 0.903 gcm^{-3}.

The microthermometric data collected from primary inclusions in prograde garnet skarn samples were pressure corrected using the estimated emplacement depth of the Tongon granodiorite, equivalent to a pressure of 2 ± 0.5 kbar. This pressure estimate is in agreement with retrograde stage 3 mineral assemblages, with prehnite forming at pressures less than 3 kbar (Willner et al., 2009, 2013). Assuming minimal uplift between the time of skarn development and the emplacement of the Tongon granodiorite, trapping temperatures for the stage 2 prograde skarn fluids were estimated using the isochore method of Roedder and Bodnar (1984). Pressure corrected trapping temperatures for fluid inclusions in stage 2 garnet are estimated to have been between 470° and 685°C (Fig. 15).

Sulfur isotopes

Sulfur isotope ratios were analyzed from 10 mineralized stage 3 samples. The mineral separates included pyrrhotite II and pyrite but no arsenopyrite due to the fine-grained nature of this sulfide phase and contamination from löllingite cores. Tongon pyrite and pyrrhotite $\delta^{34}S$ values range from –3 to 0.7‰ with a mean of –1.1 ± 1.3‰ (Fig. 16). One outlying sample has a $\delta^{34}S$ value of –5‰. Pyrrhotite has lower $\delta^{34}S$ values (*n* = 3; –5 to –2‰ with mean of –3 ± 1.7‰) than paragenetically earlier pyrite (*n* = 7; –3 to 0.7‰ with mean of –0.8 ± 1.4‰). No clear variation in $\delta^{34}S$ values is seen between samples from Tongon South (*n* = 6; –2.7 to –0.2‰ with mean of –1.2 ± 1.1‰) and Tongon North (*n* = 4; –5–0‰ with mean of –1.8 ± 2.6‰).

Discussion

Although the Tongon deposits lack the classical replacement of carbonates and intrusions, they are classified as skarns because the alteration system is dominated by calc-silicate minerals (see Meinert, 1998; Meinert et al., 2005). Here we discuss the data outlined above and develop a model for these deposits, which differ markedly from other major Paleoproterozoic orogenic Au deposits in West Africa (Oberthür et al., 1996, 1998; Lawrence et al., 2013a, 2016; Treloar et al., 2014; Lambert-Smith et al., 2016; Markwitz et al., 2016).

Skarn replacing basaltic-andesitic rocks

The majority of skarn deposits reported worldwide, including Au skarns, are carbonate-hosted and form proximal to epizonal Phanerozoic intrusions emplaced at depths <5 km (Meinert, 1998). The Tongon skarn, however, is hosted in greenschist facies Paleoproterozoic volcaniclastic rocks that lack primary carbonates and provides insights into the skarn replacement process in noncarbonate rocks. Skarn and related mineralization at Tongon South and Tongon North is hosted exclusively within basaltic-andesitic crystal tuffs (Figs. 2, 5) and is absent from all other rock types in the local stratigraphy. The basaltic-andesitic protolith of the skarns is clearly demonstrated by the presence of residual blocks of tuff in the skarns (Figs. 3, 6C-E) and by the continuity of bedding planes between zones of skarn alteration and less strongly altered basaltic-andesite tuff. It is proposed here that the skarn replacement of these mafic volcaniclastic rocks was aided by elevated F in the hydrothermal fluid, which is known to facilitate the dissolution of silicates (Chang and Meinert, 2008). Enrichment in F is indicated by the presence of accessory fluorite and fluorapatite in the stage 2 skarns.

Petrographic, mineralogical, and geochemical data highlight both protolith and external fluid-related controls on the mineralogy and composition of the skarns. Skarn that overprints the basaltic andesitic tuffs contains Al- and Ti-rich garnets ($Gr_{30–85}$; mean of Gr_{61}; TiO_2 of 0.5–1.7 wt %) (Table A1), as well as pentlandite and chromite reflecting the Ti-, Ni-, and Cr-rich composition of the host rocks, whereas skarn that overprints the more Mg-rich basaltic tuffs contains Mg-rich minerals such as forsterite, tremolite, and phlogopite (Table 2). However, isocon/mass balance analyses (Fig. 8) and the mineralogy of the skarns indicate alteration resulted in significant gains in CaO, MnO, H_2O, As, S, and F from the hydrothermal fluid, independent of the composition of the protolith. The overall calc-magnesian composition of the skarn at Tongon is reflected in the grossular composition of garnet and the abundance of diopsidic clinopyroxene (Fig. 9; Table A1) and is similar to calc-magnesian character of skarns hosted by mafic volcanic rocks such as those in western British Columbia (Meinert, 1984). These skarns typically have lower Fe contents than skarns hosted by carbonate rocks (e.g., Meinert, 1998; and references therein).

The strong lithological control on the distribution of the skarn is clearly illustrated at Tongon North, where skarn development is absent from the footwall carbonaceous shales and hanging wall dacitic lapilli tuffs (Fig. 5). Skarns generally do not replace carbonaceous rocks, as oxidation of organic C forms CO_2, which suppresses skarn-forming reactions (Changand Meinert, 2008). The absence of skarn alteration in the lapilli dacitic tuffs is presumably due to the lower Ca, Mg, and Fe contents of these rocks relative to the more mafic basalticandesite tuffs that host skarn.

The calc-silicate replacement at Tongon is considered to be solely metasomatic and not a product of high-grade metamorphism (Tomkins et al., 2004; Phillips and Powell, 2009, 2010). The strong temporal and spatial zonation patterns within the skarn alteration assemblages, the lack of CO_2 in the fluid inclusions, and peak greenschist facies metamorphism throughout most of the Senoufo belt are inconsistent with a metamorphic origin for the Tongon calc-silicate assemblage.

Skarn zonation

The skarn paragenesis documented at Tongon is typical of Au skarns: (1) early potassic (stage 1) metasomatism overprinted by (2) coarser-grained prograde pyroxene-garnet replacement (stage 2) and later (3) retrogade alteration with sulfide-Au mineralization (stage 3) (Meinert, 1998; Meinert et al., 2005). The west-to-east zonation pattern of proximal garnet-pyroxene (zone A), intermediate Mg-rich pyroxene (zone B), and distal Fe-rich, pyroxene-amphibole (zone C) (Table 1; Figs. 2, 5, 9) is a characteristic feature of skarn deposits and reflects a decrease in temperature and Al-solubility in the hydrothermal fluid at progressively greater distances from the fluid source and principal fluid pathways (Meinert, 1997; Chang and Meinert, 2008). At both Tongon deposits, mineral zonation patterns imply the source of the skarn-forming fluids and/or main fluid pathway was to the west, in the area now occupied by the younger Tongon granodiorite. The contact between the stage 2 proximal garnet-bearing skarn (zone A) and intermediate diopside skarn (zone B) marks the western limit of the later retrograde Au mineralization associated with stage 3 silica-sulfide alteration (Fig. 2). This spatial correlation between the highest Au grades and more intermediate-to-distal alteration zones within the wider skarn has been reported in many Au skarns (Meinert, 2000).

Fluid chemistry and P-T conditions

Two fluid inclusion populations were recognized in stage 2 garnet and pyroxene (Fig. 14). The minor set of isolated primary H_2O-NaCl-$CaCl_2$ inclusions in garnet crystal cores, which have moderate salinities (8–14.3 wt % NaCl equiv) and estimated trapping temperatures of 470° and 685°C (Fig. 15), are thought to have been responsible for prograde skarn development at Tongon. The second group of more common H_2O-NaCl-$CaCl_2$ inclusions, which have lower salinities (0.4–5 wt % NaCl equiv) and homogenization temperatures (150°–315°C), are inferred to be related to the retrograde stage 3 replacement.

The wider range of homogenization temperatures (130°–390°C) and salinities (0.4–12.5 wt % NaCl equiv) measured in aqueous inclusions in stage 3 auriferous silica-altered samples (Fig. 14B-D) is likely the result of reequilibration of the inclusions postentrapment as the host quartz is widely recrystallized (Bodnar, 2003). In the absence of reliable trapping temperatures from stage 3 quartz-hosted fluid inclusions, the temperature of Au mineralization at Tongon was estimated using the

arsenopyrite geothermometry of Kretschmar and Scott (1976) and Sharp et al. (1985), resulting in a mean temperature of 400° to 470°C (mean As of 34.1 at. % ± 1.1%) (Table A1). The P-T formation estimates for Tongon are similar to those reported for the greenstone-hosted Nevoria Au skarn deposit in Western Australia (Mueller et al., 2004).

The oxidation state of the Tongon skarn system can be inferred from the relative proportions of the calc-silicate minerals and the mineralogy of silicate, oxide, and sulfide phases (Meinert, 1998, 2000). Ore and alteration mineral assemblages imply that Tongon is a relatively reduced skarn. Evidence for this includes the following: (1) low garnet-pyroxene ratio of ~1:10 (oxidized skarns tend have ratios of 3:1 to 20:1); (2) a lack of Fe^{+3} in garnet, resulting in grossular predominating over andradite; (3) largely intermediate diopside-hedenbergite compositions ($Di_{26–82}$, $Hd_{18–73}$); (4) the dominance of pyrrhotite over pyrite; and (5) the lack of magnetite and hematite. Löllingite is frequently observed rimmed or partially replaced by arsenopyrite (Fig. 11A-B), a texture which is consistent with cooling and reaction between pyrrhotite and löllingite (Nörtemann, 1997; Tomkins and Mavrogenes, 2001).

Within the Paleoproterozoic rocks of West Africa, high temperature, moderately saline, aqueous, reduced, mineralizing fluids, similar to those responsible for skarn formation at Tongon, have only been reported from the Morila reduced intrusion-related Au deposit in Southern Mali (Hammond et al., 2011). These fluids are distinctly different from the CO_2-rich metamorphic hydrothermal fluids responsible for orogenic Au mineralization across much of the craton (Schwartz et al., 1992; Schmidt Mumm et al., 1997; Yao et al., 2001; Lawrence et al., 2013b; Lambert-Smith et al., 2016).

Controls on the location and origin of the Tongon skarns

The location of the Tongon Au skarns within the zone of E to ENE-striking faults that cut across the N- to NE-striking structural grain of the Senoufo belt implies these faults were a key control on the location of the Tongon deposits (Fig. 1). This is especially evident at Tongon North, where auriferous skarn is located in a planar zone adjacent to one of the largest of the E- to ENE-striking faults (Fig. 5). These deposit and district-scale relationships imply the E-ENE–striking faults were the principal conduits that focused the movement of skarn-forming hydrothermal fluids. Developing an understanding of their origin and likely depth extent is therefore a key aspect of any genetic model that attempts to explain the source of the Tongon Au skarns.

The zone of E- to ENE-striking faults that host the Tongon skarn deposits forms part of a much more extensive fault system, which includes several regional-scale N- to NE-striking reverse faults that extend throughout the Senoufo belt (Fig. 1). These N- to NE-striking faults are orogen-parallel faults formed during Eburnean NW-SE compression (e.g., Allibone et al., 2002a; de Kock et al., 2011; Perrouty et al., 2012). The N- to NE-striking faults appear to link with either end of the zone of E- to

ENE-striking faults. This implies that the latter are part of a major steeply dipping transfer zone within the wider Eburnean fault system that extends throughout the belt. To date no Au skarns have been found along the N- to NE-striking parts of this fault system, only the E- to ENE striking corridor, implying the melt and/or fluid source of the skarns were only able to access the midcrust through the E- to ENE-striking faults.

Similar orogen-oblique transfer fault systems have been cited as controls on the location of some porphyry deposits (e.g., Gow and Walshe, 2005), polymetallic skarns (McCuaig and Hronsky, 2014), and other types of gold deposits (Hronsky et al., 2012). These transfer fault systems are thought by some to extend through the full thickness of the crust, providing pathways through which melts formed in the deep crust and even the upper mantle and may have accessed the mid and upper crust. In addition, any lower-temperature fluids exsolved during melt emplacement in the mid- and upper crust (e.g., Rock et al., 1987; Blewett and Hall, 2009; Mole et al., 2013). The occurrence of primitive magmatic rocks, such as ferroan granites and lamprophyre dikes, along the E to ENE-striking faults in the vicinity of Tongon (Figs. 1, 5) implies that these orogen-oblique transfer faults are potentially translithospheric in scale. The relatively high temperature of the skarn-forming fluid at Tongon, compared to the ambient greenschist facies conditions in the surrounding volcano-sedimentary rocks, is consistent with a proximal magmatic fluid source emplaced in the mid rather than upper crust. This is in agreement with δ34S data collected from stage 3 sulfides (–3–0.7‰) (Ohmoto and Rye, 1979). The lack of Bi- and Te-bearing minerals distinguishes the Tongon Au skarn from many epizonal Au skarns associated with hypabyssal intrusive rocks emplaced at shallower depths (e.g., Cockerton and Tomkins, 2012). The structural setting of the Tongon Au skarns imply that similar large (>30 Mt) Au skarns hosted in metamorphic terranes may occur where major orogen-oblique transfer faults are also present.

Implications for regional metallogeny

Radiometric dating of the Tongon Au skarn at 2134 ± 21 Ma indicates that mineralization formed during the early parts of the Eburnean orogeny, 20 to 70 m.y. before the major episode of orogenic Au mineralization in southwest Ghana and western Mali (Oberthür et al., 1998; White et al., 2014; Markwitz et al., 2016; Masurel et al 2017), and 0 to 40 m.y. after the Wassa Au deposit in southwest Ghana (Perrouty et al., 2015, 2016; Markwitz et al., 2016). The comparatively old age of the Tongon Au skarn deposits is further evidence that Au mineralization within the Paleoproterozoic rocks of West Africa occurred over several tens of millions of years through a variety of different processes, rather than in a single major pulse of orogenic Au mineralization near the end of Paleoproterozoic tectonism and plutonism. Other reported examples of Au skarn mineralization in the Paleoproterozoic rocks of West Africa include the Ity deposit in the Toulepleu-Ity outlier in western Côte d'Ivoire (Tabaud et al.,

2015; Béziat et al., 2016), and minor Au occurrences in the southern and central parts of the Siguiri basin in Guinea (Feybesse et al., 2004; Vic and Billa, 2015). These skarns are all carbonate-hosted and form proximal to causative plutons.

Conclusions

The structural, geochronological, mineralogical, and chemical data set out in this paper provide an insight into the geologic history of the Tongon Au skarn deposit, which had previously been poorly understood. Gold skarn mineralization at Tongon is located along a corridor of orogen-oblique ENE-striking faults. No skarn occurrences have been observed outside of this corridor along the orogen-parallel N- to NNE-striking reverse faults that dominate the structure of the Senoufo belt. This observation implies that the source of the skarns was only able to access the midcrust through the ENE-striking faults, and thus similar orogen-oblique faults may be prospective sites for Au skarn mineralization elsewhere across the craton.

Despite the obvious structural control on the distribution of the Tongon skarns, skarn replacement of the Senoufo stratigraphy was selective and confined to basaltic-andesitic crystal tuffs. The chemistry of the skarns was thus strongly influenced by the composition of the host rocks. Nevertheless, mineral zonation patterns, alteration paragenesis, and ore fluid chemistry recorded at Tongon are typical of Au skarns and contrast with Au mineralization elsewhere in the West African craton, which have generally been classified as orogenic Au systems. Radiometric dating of the Tongon deposit shows that skarn mineralization formed early in the Eburnean orogeny, around ~2140 Ma. The skarn formed prior to the onset of region-wide orogenic Au mineralization (ca. 2100–2060 Ma), which manifest as closely spaced deposits concentrated in linear belts mainly in the northwestern and eastern parts of the craton. Although the distribution and timing of the various Au deposit styles across the craton is still not fully understood, the data presented here and in other recent publications (e.g., Perrouty et al., 2015, 2016; Markwitz et al., 2016) imply that distinct metallogenic epochs occur within the 2.2 to 2.0 Ga Birimian province.

Acknowledgments

The authors would like to acknowledge C. French (Kingston University London) for participation in some of the sample collecting and stable isotope sample preparation. The support of past and present Randgold geologists, namely A. Smeesters, D. Senghor, S. Rennie, M. Phillips and G. Viljoen, is greatly appreciated. Richard Giddens (Kingston University) is acknowledged for his assistance in electron microprobe analysis. A special thanks goes the technical staff at SUERC, East Kilbride, and University of Tasmania geochronology laboratory for their assistance with stable isotope and geochronology

analysis and interpretation, respectively. I. McDonald at Cardiff University is acknowledged for whole rock geochemical analysis of the Tongon samples. Lastly, critical reviews by L. Meinert and A. Tomkins are greatly appreciated.

REFERENCES

Abouchami, W., Boher, M., Michard, A., and Albarede, F., 1990, A major 2.1 Ga event of mafic magmatism in West Africa: An early stage of crustal accretion: Journal of Geophysical Research, v. 95, p. 17,605–17,629.

Allen, C.M., and Campbell, I.H., 2012, Identification and elimination of a matrix-induced systematic error in LA-ICP-MS 206Pb/238U dating of zircon: Chemical Geology, v. 332, p. 157–165.

Allibone, A., 2013, Geology of the Tongon gold deposit, Senoufo belt, and some exploration implications: Randgold Resources Ltd internal company report, July, 73 p.

Allibone, A., McCuaig, T.C., Harris, D., Etheridge, M., Munroe, S., Byrne, D., Ammanor, J., and Gyapong, W., 2002a, Structural controls on gold mineralization at the Ashanti deposit, Obuasi, Ghana: Society of Economic Geologists, Special Publication 9, p. 65–92.

Allibone, A., Teasdale, J., Cameron, G., Etheridge, M., Uttley, P., Soboh, A., Appiah-Kubi, J., Adanu, A., Arthur, R., Mamphey, J., Odoom, B., Zuta, J., Tsikata, A., Pataye, F., Famiyeh, S., and Lamb, E., 2002b, Timing and structural controls on gold mineralization at the Bogoso gold mine, Ghana, West Africa: Economic Geology, v. 97, p. 949–969.

Baker, J., Peate, D., Waight, T., and Meyzen, C., 2004, Pb isotopic analysis of standards and samples using a 207Pb/204Pb double spike and thallium to correct for mass bias with a double-focusing MC-ICP-MS: Chemical Geology, v. 211, p. 275–303.

Bakker, R.J., 2003, Package FLUIDS 1. Computer programs for analysis of fluid inclusion data and modeling bulk fluid properties: Chemical Geology, v. 194, p. 3–23.

Ballo, I., Traore, A., Sanogo, L., Daou, G., Guindo, B., Ouologuem, Y., and Hein, K.A.A., 2016, The Syama and Tabakoroni goldfields, Mali: Ore Geology Reviews, v. 78, p. 578–585.

Baratoux, L., Metelka, V., Naba, S., Ouiya, P., Siebenaller, L., Jessell, M.W., Narég, A., Salvi, A., Béziat, D., and Franceschi, G., 2015, Tectonic evolution of the Gaoua region, Burkina Faso: Implications for mineralization: Journal of African Earth Science, v. 112, p. 419–439.

Best, F.C., 2012, The petrogenesis and Ni-Cu-PGE potential of the Dido batholith, North Queensland, Australia: Ph.D thesis, Hobart, University of Tasmania, 269 p.

Béziat, D., Siebenaller, L., Salvi, S., and Chevalier, P., 2016, A weathered skarn-type mineralization in Ivory Coast: The Ity gold deposit: Ore Geology Reviews, v. 78, p. 724–730.

Black, L.P., Kamo, S.L., Allen, C.M., Davis, D.W., Aleninikoff, J.N., Valley, J.W., Mundil, R., Campbell, I.H., Korsch, R.J., Williams, I.S., and Foudoulis, C., 2004, Improved $^{206}Pb/^{238}U$ microprobe geochronology by the monitoring of a trace-element related matrix effect; SHRIMP, ID-TIMS, ELA-ICP-MS, and oxygen isotope documentation for a series of zircon standards: Chemical Geology, v. 205, p. 115–140.

Blewett, R.S., and Hall, G., 2009, Mineral systems and large scale exploration targeting: The lessons from the PMD-CRC Yilgarn projects, *in* Williams, P.J., et al., eds., Smart science for exploration and mining: Proceedings of the 10th biennial meeting of the Society for Geology Applied to Mineral Deposits (SGA), Townsville, Australia, James Cook, p. 87–88.

Bodnar, R.J., 2003, Reequilibration of fluid inclusions. Fluid inclusions: Analysis and interpretation, v. 32, p. 213–230.

Bodnar, R.J., and Vityk, M.O., 1994, Interpretation of microthermometric data for H_2O-NaCl fluid inclusions, *in* De Viro, B., and Frezzotti, M.I, eds., Fluid inclusions in minerals: Methods and applications: Blacksburg, Virginia, Virginia Tech, p. 117–130.

Brooks, S., and Cameron, G., 2009, Banfora discovery: A granite-hosted Birimian gold deposit in southwestern Burkina Faso: NewGenGold 2009: Case histories of discovery, Perth, Australia, November 23-24, 2009, Proceedings, p. 217–231.

Chang, Z., and Meinert, L.D., 2008, Zonation in skarns—complexities and controlling factors: Pacific Rim Congress, 11th, Gold Coast, QLD, Australia, November 24-26, 2008, p. 303–306. Proceedings, p. 303–306.

Chang, Z., Vervoort, J.D., McClelland, W.C., and Knaack, C., 2006, U-Pb dating of zircon by LA-ICP-MS: Geochemistry, Geophysics, Geosystems, v. 7, p. 1–14.

Chew, D.M., Sylvester, P.J., and Tubrett, M.N., 2011, U-Pb and Th-Pb dating of apatite by LA-ICPMS: Chemical Geology, v. 280, p. 200–216.

Cockerton, A.B.D., and Tomkins, A.G., 2012, Insights into the liquid bismuth collector model through analysis of the Bi-Au Stormont skarn prospect, northwest Tasmania: Economic Geology, v. 107, p. 667–682.

Davis, D.W., Lowenstein, T.K., and Spencer, R.J., 1990, Melting behaviour of fluid inclusions in laboratory-grown halite crystals in the systems NaCl-H_2O, NaCl-KCl-H_2O, NaCl-$MgCl_2$-H_2O, and NaCl-$CaCl_2$-H_2O: Geochimica et Cosmochimica Acta, v. 54, p. 591–601.

Doumbia, S., Pouclet, A., Kouamelan, A., Peucat, J.J., Vidal, M., Delor, C., 1998, Petrogenesis of juvenile-type Birimian (Palaeoproterozoic) granitoids in central Côte-d'Ivoire, West Africa: Geochemistry and geochronology: Precambrian Research, v. 87, p. 33–63.

de Kock, G.S., Armstrong, R.A., Siegfried, H.P., and Thomas, E., 2011, Geochronology of the Birim Supergroup of the West African craton in the Wa-Bolé region of west central Ghana: Implications for the stratigraphic framework: Journal of African Earth Sciences, v. 59, p. 1–40.

Droop, G.T.R., 1987, A general equation for estimating Fe^{3+} concentrations in ferromagnesian silicates and oxides from microprobe analyses, using stoichiometric criteria: Mineralogical Magazine, v. 51, p. 431–435.

Feybesse, J.L., Billa, M., Diaby, S., Diallo, S., Egal, E., Le Metour, J., Lescuyer, J.L., Sylla, B.I., and Villeneuve, M., 2004, Notice explicative de la Carte Géologique et Gitologique à 1/500 000 de la Guinée: Bureau de Recherches Géologiques et Minières (BRGM), Recherche Géologique et des Hydrocarbures (DNRGH), p 60.

Gow, P.A., and Walshe, J.L., 2005, The role of preexisting geologic architecture in the formation of giant porphyry-related Cu +/- Au deposits: Examples from New Guinea and Chile: Economic Geology, v. 100, p. 819–833.

Grant, J.A., 1986, The isocon diagram—a simple solution to Gresens' equation for metasomatic alteration: Economic Geology, v. 81, p. 1976–1982.

Halpin, J.A., Jensen, T., McGoldrick, P., Meffre, S., Berry, R.F., Everard, J.L., Calver, C.R., Thompson, J., Goemann, K., and Whittaker, J.M., 2014, Authigenic monazite and detrital zircon dating from the Proterozoic Rocky Cape Group, Tasmania: Links to the Bel-Purcell Supergroup, North America: Precambrian Research, v. 250, p. 50–67.

Hammarstrom, J.M., and Zen, E.A., 1986, Aluminium in hornblende: An empirical igneous geobarometer: American Mineralogist, v. 71, 1297–1313.

Hammond, N.Q., Robb, L., Foya S., and Ishiyama, D., 2011, Mineralogical, fluid inclusion, and stable isotope characteristics of Birimian orogenic gold mineralization at the Morila mine, Mali, West Africa: Ore Geology Reviews, v. 39, p. 218–229.

Hein, K.A.A., 2010, Succession of structural events in the Goren greenstone belt (Burkina Faso); implications for West African tectonics: Journal of African Earth Sciences, v. 56, p. 83–94.

Hein, K.A.A., Matsheka, I.R., Bruguier, O., Masurel, Q., Bosch, D., Caby, R., Monie, P., 2015, The Yatela gold deposit: Two billion years in the making: Journal of African Earth Science, v. 112, p. 548–569.

Hronsky, J.M.A., Groves, D.I., Loucks, R.R., and Begg, G.C., 2012, A unified model for gold mineralization in accretionary orogens and implications for regional-scale exploration targeting methods: Mineralium Deposita, v. 47, p. 339–358.

Jackson, S.E., Pearson, N.J., Griffin, W.L., Belousova, E.A., 2004, The application of laser ablation-inductively coupled plasma-mass spectrometry to in situ U–Pb zircon geochronology: Chemical Geology, v. 211, p. 47–69.

Klötzli, U., Klötzli, E., Günes, Z., and Kosler, J., 2009, Accuracy of laser ablation U–Pb zircon dating: Results from a test using five different reference zircons: Geostandards and Geoanalytical Research, v. 33, p. 5–15.

Knight, C.L., and Bodnar R.J., 1989, Synthetic fluid inclusions: IX. Critical PVTX properties of NaCl-H_2O solutions: Geochimica et Cosmochimica Acta, v. 54, p. 3–8.

Kretschmar, U., and Scott, S.D., 1976, Phase relations involving arsenopyrite in the system Fe-As-S and their application: Canadian Mineralogy, v. 14, p. 364–386.

Lambert-Smith, J.S., Lawrence, D.M., Herbert, S., Vargas, C.A, Boyce, A.J., and Treloar, P.J., 2016, The Gounkoto Au deposit, West Africa: Constraints on ore genesis and volatile sources from petrological, fluid inclusion and stable isotope data: Ore Geology Reviews, v. 78, p. 606-622.

Lawrence, D.M., Treloar, P.J., Rankin, A.H., Harbidge, P., and Holliday, J., 2013a, The geology and mineralogy of the Loulo mining district, West Africa: Evidence for two distinct styles of orogenic gold mineralization: Economic Geology, v. 108, p. 199–227.

Lawrence, D.M., Treloar, P.J., Rankin, A.H., Boyce, A., and Harbidge, P., 2013b, Fluid inclusion and stable isotope study at the Loulo mining district, Mali, West Africa: Implications for multi-fluid sources in the generation of orogenic gold deposits: Economic Geology, v. 108, p. 229–257.

Lawrence, D.M., Lambert-Smith, J.S., and Treloar, P.J., 2016, A review of gold mineralization in Mali, *in* Bouabdellah, M., and Slack, J.F, eds., Mineral Deposits of North Africa, Mineral Resource Reviews: Springer, doi 10.1007/978-3-319-31733-5_13, p. 327–351.

Le Mignot, E., Siebenaller, L., Béziat, D., André-Mayer, A-S., Reisberg, L., Salvi, S., Velásquez, G., Zimmermann, C., and Naré, A., 2017, The Paleoproterozoic copper-gold deposit of Gaoua, Burkina Faso: Super-positon of orogenic gold on a porphyry copper occurrence? Economic Geology, v. 112, p. 99–122.

Markwitz, V., Hein, K.A.A., and Miller, J.M., 2016, Compilation of West African mineral deposits: Spatial distribution and mineral endowment: Precambrian Research, v. 274, p. 61–81.

Masurel, Q., Miller, J., Hein, K.A.A., Hanssen, E., Thébaud, N., Ulrich, S., Kaisin, J., and Tessougue, S., 2016, The Yatela gold deposit in Mali, West Africa: The final product of a long-lived history of hydrothermal alteration and weathering: Journal of African Earth Science, v. 113, p. 73–87.

Masurel, Q., Thébaud, N., Miller, J., Ulrich, S., Hein, K.A.A., Cameron, G., Béziat, D., Bruguier, O., and Davis, J.A., 2017, Sadiola Hill: A world-class carbonate-hosted gold deposit in Mali, West Africa: Economic Geology, v. 112, p. 23–47.

McCuaig, T.C., and Hronsky, J.M.A., 2014, The minerals system concept: The key to exploration targeting: Society of Economic Geologists, Special Publication 18, p. 153–175.

McFarlane, C.M., Mavrogenes, J., Lentz, D., King, K., Allibone, A., and Holcombe, R., 2011, Geology and intrusion-related affinity of the Morila gold mine, Southeast Mali: Economic Geology, v. 106, p. 727–750.

Meinert, L.D., 1984, Mineralogy and petrology of iron skarns in western British Columbia, Canada: Economic Geology, v. 79, p. 869–882.

——1997, Application of skarn deposit zonation models to mineral exploration: Exploration and mining geology, v. 6, p. 185–208.

——1998, A review of skarns which contain gold: Mineralogical Association of Canada Short Course Series, v. 26, p. 359–414.

——2000, Gold in skarns related to epizonal intrusions: Reviews in Economic Geology, v. 13, p. 347–375.

Meinert, L.D., Dipple, G.M., and Nicolescu, S., 2005, World skarn deposits: Economic Geology 100th Anniversary volume, p. 299–335.

Mole, D.R., Fiorentini, M.L., Cassidy, K.F., Kirkland, C.L., Thebaud, N., McCuaig, T.C., Doublier, M.P., Duuring, P., Romano, S.S., Maas, R., Belousova, E.A., Barnes, S.J., and Miller, J., 2013, Crustal evolution, Intracratonic architecture, and the metallogeny of an Archaean craton: Geological Society of London Special Publication, v. 393, p.23–80.

Mueller, A.G., 1997, The Nevoria gold skarn deposit in Archean iron-formation, Southern Cross greenstone belt, Western Australia: 1. Tectonic setting, petrography, and classification: Economic Geology, v. 92, p. 181–209.

Mueller, A.G., Nemchin, A.A., and Frei, R., 2004, The Nevoria gold skarn deposit in Archean iron-formation, Southern Cross greenstone belt, western Australia: 2. Pressure-temperature-time path and relationship to postorogenic granites: Economic Geology, v. 99, p. 453–478.

Nörtemann, M.F-J., 1997, Part I: Geological Mapping of the Aukuppe Area on the Farms Otjimbojo and Otjakatjongo in the Central Damara Orogen, Namibia. Part II: Genesis, Petrography and Mineral Chemistry of the Gold skarn Deposit Navachab in the Central Damara Orogen, Namibia. M.S. thesis, University of Göttingen, Göttingen, Germany, 265 p.

Oberthür, T., Schmidt Mumm, A., Vetter, U., Simon, K., and Amanor, J.A., 1996, Gold mineralization in the Ashanti belt of Ghana: Genetic constraints of the stable isotope geochemistry: Economic Geology, v. 91, p. 289–301.

Oberthür, T., Vetter, U., Davis, D.W., and Amanor, J.A., 1998, Age constraints on gold mineralization and Paleoproterozoic crustal evolution in the Ashanti belt of southern Ghana: Precambrian Research, v. 89, p. 129–143.

Ohmoto, H., and Rye, R.O., 1979, Isotopes of sulfur and carbon, *in* Barnes, H. I., ed., Geochemistry of hydrothermal ore deposits, 2nd ed., New York, Wiley, p. 509–567.

Olson, S.F., Diakite, K., Ott, L., Guindo, A., Ford, C.R.B., Winer, N., Hanssen, E., Lay, N., Bradley, R., and Pohl, D., 1992, Regional setting, structure, and descriptive geology of the Middle Proterozoic Syama gold deposit, Mali, West Africa: Economic Geology, v. 87, p. 310–331.

Pan, Y., Fleet, M.E., and Stone, W.E., 1991, Skarn mineralization (Cr, Fe, Au) in an Archean greenstone belt, White River Property, Helmo area, Ontario: Economic Geology, v. 86, p. 1626–1645.

Perrouty, S., Aillères, L., Jessell, M.W., Baratoux, L., Bourassa, Y., and Crawford, B., 2012, Revised Eburnean geodynamic evolution of the gold-rich southern Ashanti belt, Ghana, with new field and geophysical evidence of pre-Tarkwaian deformations: Precambrian Research, v. 204, p. 12–39.

Perrouty, S., Jessell, M.W., Bourassa, Y., Miller, J., Apau, D., Siebenaller, L., Velásquez, G., Baratoux, L., Aillères, L., Béziat, D., and Salvi, S., 2015, The Wassa deposit: A polydeformed orogenic gold system in southwest Ghana—implications for regional exploration: Journal of African Earth Science, v. 112, p. 536–547.

Perrouty, S., Jessell, M.W., Bourassa, Y., Miller, J., Apau, D., Parra-Avilla, L., Le Mignot, E., Velásquez, G., Ganne, J., Siebenaller, L., Baratoux, L., Aillères, L., Andre-Mayer, A,S., Béziat, D., and Salvi, S., 2016, Geological setting of the Wassa gold deposit, southwest Ghana: Ore Geology Reviews, v. 78, p. 687–691.

Phillips, G.N., and Powell, R., 2009, Formation of gold deposits: Review and evaluation of the continuum model: Earth Science Reviews, v. 94, p. 1–21.

——2010, Formation of gold deposits: A metamorphic devolatilisation model: Journal of Metamorphic Geology, v. 28, p. 689–718.

Robinson, B.W., and Kusakabe, M., 1975, Quantitative preparation of SiO_2 for $^{34}S/^{32}S$ analysis from sulfides by combustion with cuprous oxide: Analytical Chemistry, v. 47, p. 1179–1181.

Rock, N.M.S, Duller, P., Haszeldine, R.S., and Groves, D.I., 1987, Lamprophyres as potential gold exploration targets: Some preliminary observations and speculations, *in* Ho, S.E., and Groves, D.I., eds., Recent advances in understanding Precambrian gold deposits: Perth, University of Western Australia, Geology Department and University Extension, Publication 11, p. 271–286.

Roedder, E., and Bodnar, R.J., 1984, Geologic pressure determinations from fluid inclusion studies: American Reviews of Earth and Planetary Science, v. 8, p. 263–301.

Schmidt Mumm, A., Oberthur, T., and Vetter, U., 1997, High CO_2 content of fluid inclusions in gold mineralizations in the Ashanti belt, Ghana: A new category of ore forming fluids: Mineralium Deposita, v. 32, p. 107–118.

Schmitz, M.D., and Bowring, S.A., 2001, U-Pb zircon and titanite systematics of the Fish Canyon tuff: An assessment of high-precision U-Pb geochronology and its application to young volcanic rocks: Geochimica et Cosmochimica Acta, v. 65, p. 2571–2587.

Schoene, B., Crowley, J.L., Condon, D.J., Schmitz, M.D., and Bowring, S.A., 2006, Re-assessing the uranium decay constants for geochronology using ID-TIMS U–Pb data: Geochimica et Cosmochimica Acta, v. 70, p. 426–445.

Schwartz, M.O., Oberthur, T., Amanor, J., and Gyapong, E.A., 1992, Fluid inclusion re-equilibration and P-T-X constraints on fluid evolution in the Ashanti gold deposit, Ghana: European Journal of Mineralogy, v. 4, p. 1017–1034.

Sharp, Z.D., Essene, E.J., and Kelly, W.C., 1985, A re-examination of the arsenopyrite geothermometer: Pressure consideration and applications to natural assemblages: Canadian Mineralogy, v. 23, p. 517–534.

Stacey, J.S., and Kramers, J.D., 1975, Approximation of terrestrial lead isotope evolution by a two-stage model: Earth Planetary Science Letters, v. 26, p. 207–221.

Tabaud, A-S., Trap, P., Marquer, D., Durand, C., Lescuyer, J-C., and Furic, R., 2015, New insight on the magmatic and tectono-metamorphic evolution of the Paleoproterozoic gold-bearing Toulépleu-Ity district (southwest Ivory Coast): Mineral resources in a sustainable world, Society for Geology Applied to Mineral Deposits (SGA) Biennial Meeting, 13th, Nancy, France, August 2015, Proceedings, v. 4, p. 1667–1670.

Tomkins, A.G., and Mavrogenes, J.A., 2001, Redistribution of gold within arsenopyrite and löllingite during pro- and retrograde metamorphism: Application to timing of mineralization: Economic Geology, v. 96, p. 525–534.

Tomkins, A.G., Pattison, D.R.M., and Zaleski, E., 2004, The Hemlo gold deposit, Ontario: An example of melting and mobilization of a precious metal-sulfosalt assemblage during amphibolite facies metamorphism and deformation: Economic Geology, v. 99, p. 1063–1084.

Treloar, P.J., Lawrence, D.M., Senghor, D., Boyce, A., and Harbidge, P., 2014, The Massawa gold deposit, eastern Senegal, West Africa: An orogenic gold deposit sourced from magmatically derived fluids: Geological Society London, Special Publications, v. 393, p. 135–160.

Twiss, R.J., and Moores, E.M., 1992, Structural geology, New York, W.H. Freeman, 544 p.

Vic, G., and Billa, M., 2015, Geological setting and types of carbonate-hosted gold deposits in the Birimian of West Africa: Mineral resources in a sustainable world, Society for Geology Applied to Mineral Deposits (SGA) Biennial Meeting, 13th, Nancy, France, August 2015, Proceedings.

White, A., Burgess, R., Charnley, N., Selby, D., Whitehouse, M., Robb, L., and Waters, D., 2014, Constraints on the timing of late-Eburnean metamorphism, gold mineralization, and regional exhumation at Damang mine, Ghana: Precambrian Research, v. 243, p. 18–38.

Willner, A.P., Sepulveda, A.F., Herve, F., Massonne, H-J., and Sudo, M., 2009, Conditions and timing of pumpellyite actinolite-facies metamorphism in the Early Mesozoic frontal accretionary prism of the Madre de Dios Archipelago (latitude 508200S; southern Chile): Journal of Petrology, v. 50, p. 2127–2155.

Willner, A.P., Massonne, H-J., Barr, S.M., and White, C.E, 2013, Very low to low-grade metamorphic processes related to the collisional assembly of Avalonia in southeast Cape Breton Island (Nova Scotia, Canada): Journal of Petrology, v. 54, p. 1849–1874.

Yang, Z., Chang, Z., Hou, Z., and Meffre, S., 2015, Age, igneous petrogenesis, and tectonic setting of the Bilihe gold deposit, China, and implications for regional metallogeny: Gondwana Research, v. 34, p. 296–314.

Yao, Y., Murphy, P.J., Robb, L.J., 2001, Fluid characteristics of granitoid-hosted gold deposits in the Birimian terrane of Ghana: A fluid inclusion microthermometric and Raman spectroscopic study: Economic Geology, v. 96, p. 1611–1643.

Zhang, Y.G., and Frantz, J.D., 1987, Determination of homogenization temperatures and densities of supercritical fluids in the system NaCl-KCl-$CaCl_2$-H_2O using synthetic fluid inclusions: Chemical Geology, v. 64, p. 335–350.

Figures

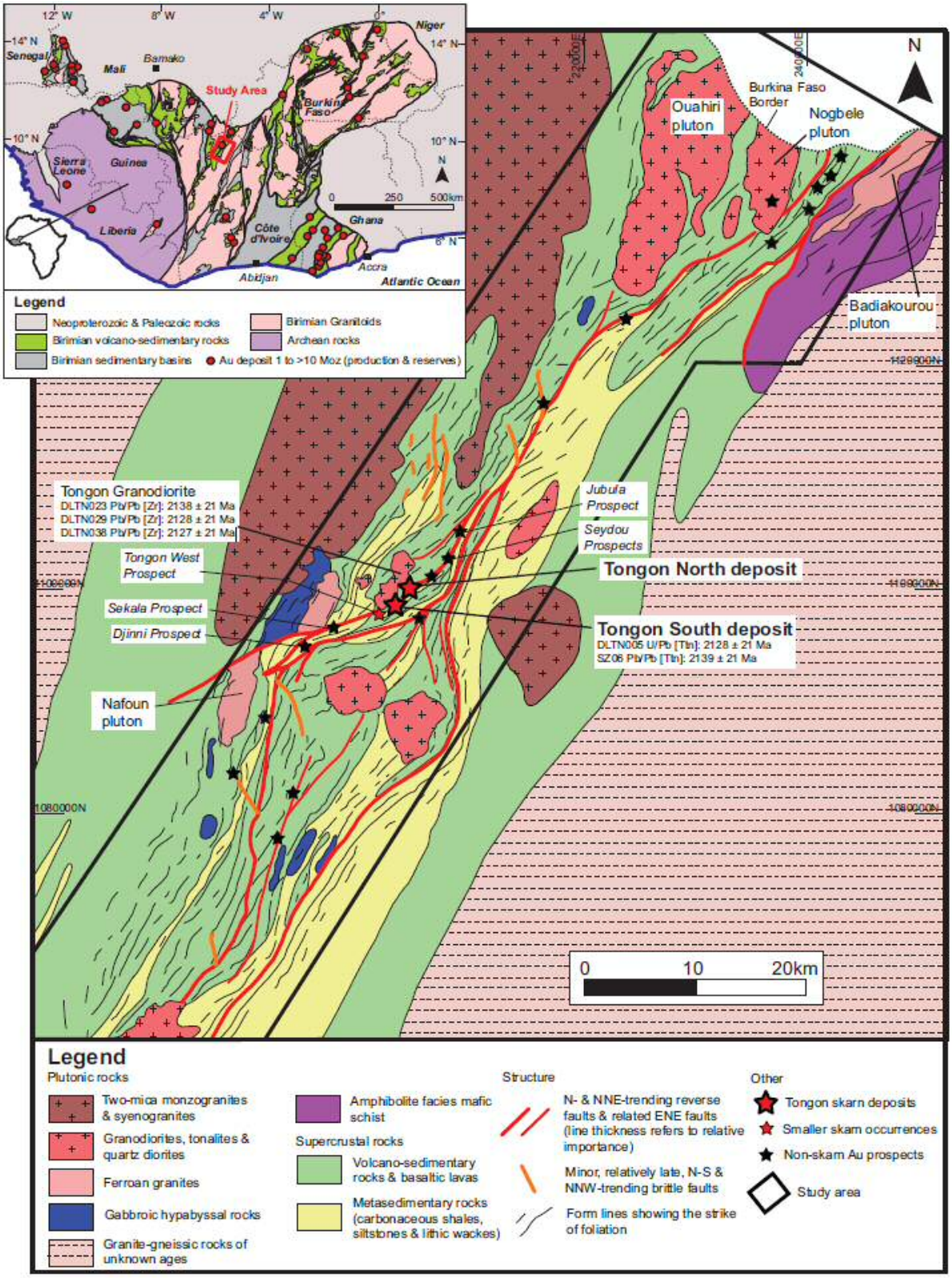

Figure 1 Regional geology map of the Senoufo belt in northern Côte d'Ivoire. Grid coordinates = WGS 84 N UTM zone 30. Inset map: geologic map of the southern West African craton showing the location of major gold deposits (>1 Moz). The study area is highlighted by the red box on the inset figure. Abbreviations: Tth = titanite dating, Zr = zircon dating.

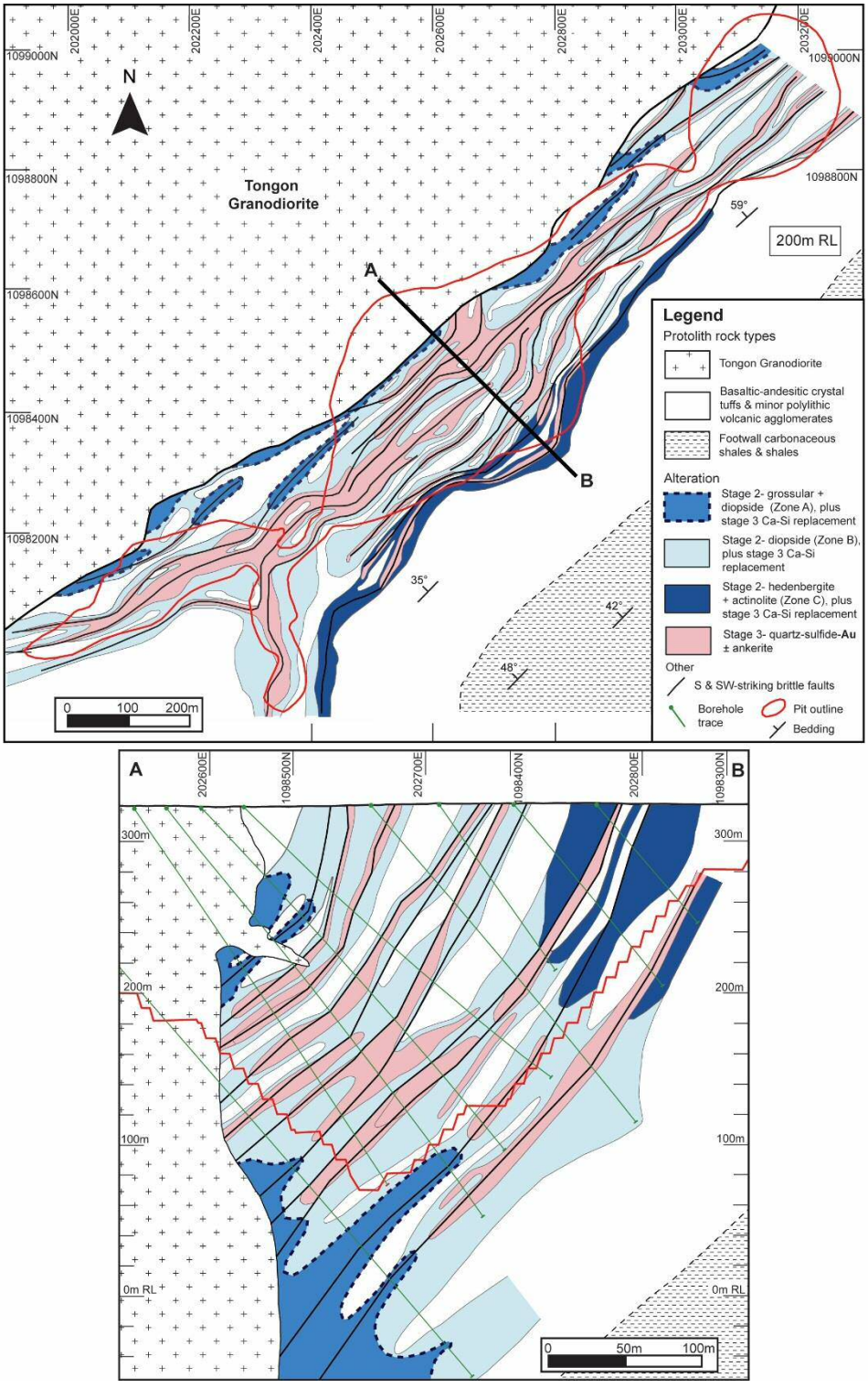

Figure 2 Typical flitch map (200 m RL) and cross section (A-B) of the Tongon South deposit, showing lithology, structure, and distribution of skarn. The extent of the stage 1 K alteration is not well constrained, although it is absent from the footwall shales and carbonaceous shales. The minor phase of late (stage 4) chlorite-sericite alteration is not shown. Note the plan and section images are a different scale. Abbreviations: Ab = albite, Act = actinolite, Ank = ankerite, Cc = calcite, Czo = clinozoisite, Di = diopside, Ep = episote, Hd = hedenbergite, Gr = grossular garnet, Pmp = pumpellyite, Prh = prehnite, Qtz = quartz.

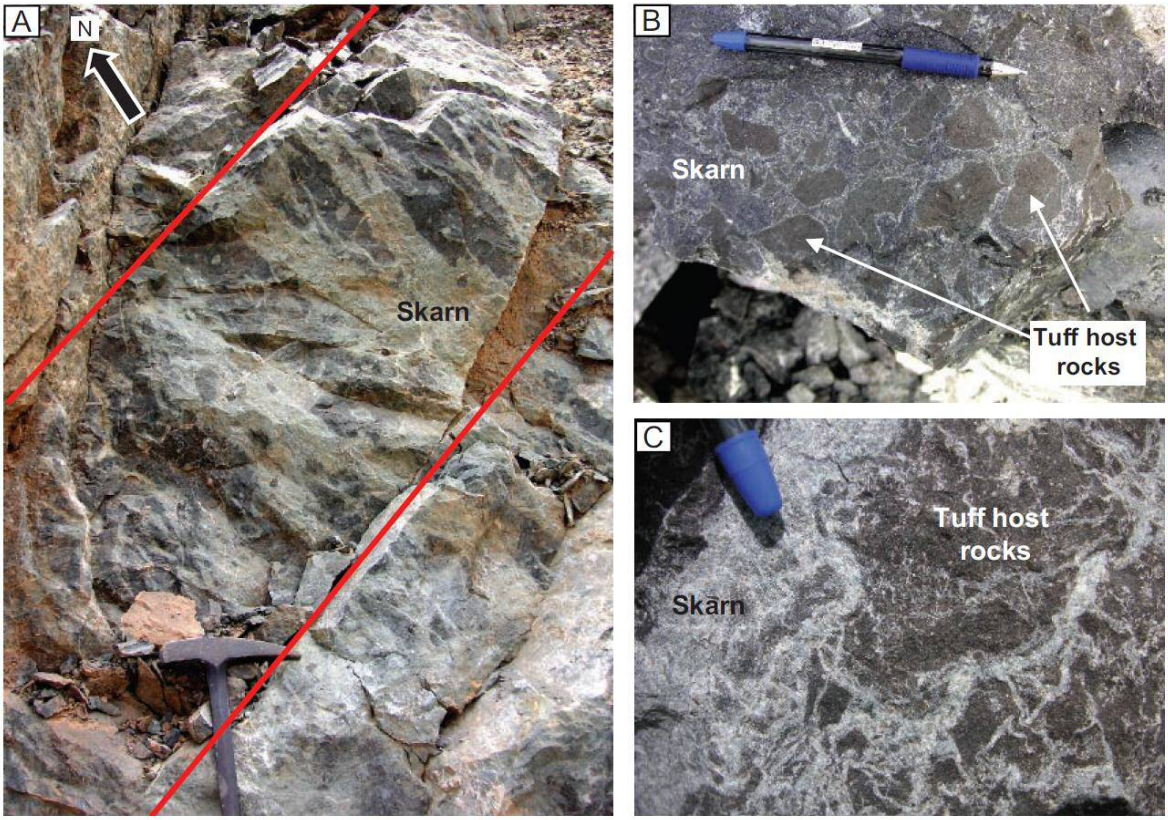

Figure 3 Photographs showing the Tongon South deposit-scale brittle structures (red lines in A) and associated skarn (A-C) overprinting the basaltic-andesitic tuffs. The brecciation is largely caused by skarn replacement of the host rocks (pseudobreccias). The light-colored skarns shown in these photos are largely dominated by diopside and later replacement phases of epidote and prehnite.

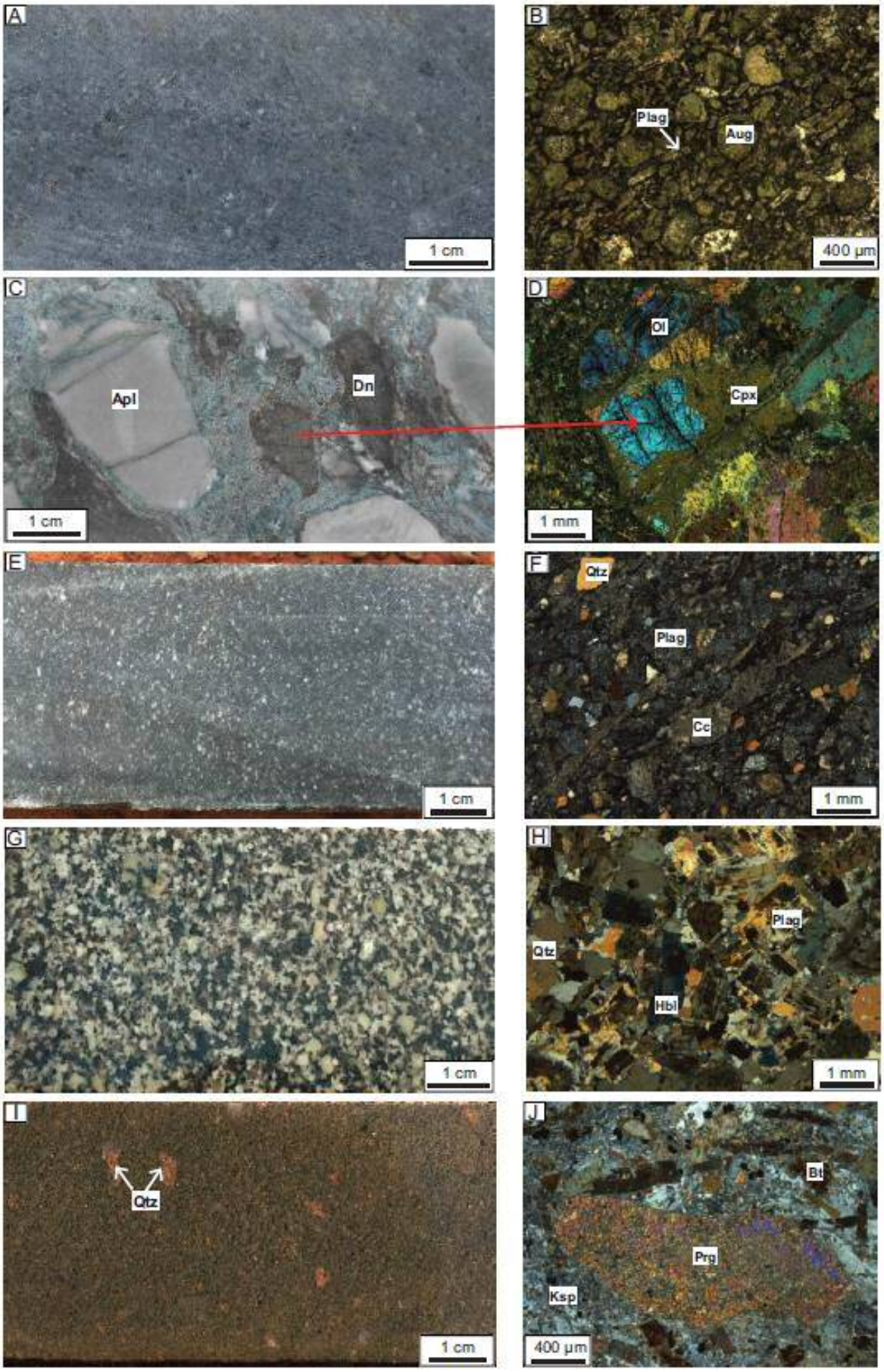
A
1 cm
B
Plag
Aug
400 µm
C
Apl
Dn
1 cm
D
Ol
Cpx
1 mm
E
1 cm
F
Qtz
Plag
Cc
1 mm
G
1 cm
H
Plag
Qtz
Hbl
1 mm
I
Qtz
1 cm
J
Bt
Prg
Ksp
400 µm

Figure 4 Hand specimen photographs and photomicrographs of the main lithologies in the Tongon district. (A-B) Basaltic-andesitic crystal tuffs. (C-D) Coarse polylithic volcaniclastic rocks, with clasts of leucocratic aplite and darker ultramafic material. These rocks also contain clasts of porphyritic felsic intrusive material and carbonaceous shales, which are not shown here. (E-F) Dacitic, lapilli, welded tuff from the hanging wall at Tongon North. (G-H) Medium-grained, hornblende-bearing Tongon granodiorite. (I-J) Least-altered example of the medium-grained lamprophyric dikes. Abbreviations: Apl = aplite, Aug = augite, Bt = biotite, Cc = calcite, Cpx = clinopyroxene, Dn = dunite, Hbl = hornblende, Ksp = K-feldspar, Ol = olivine, Plag = plagioclase, Prg = pargasite, Qtz = quartz.

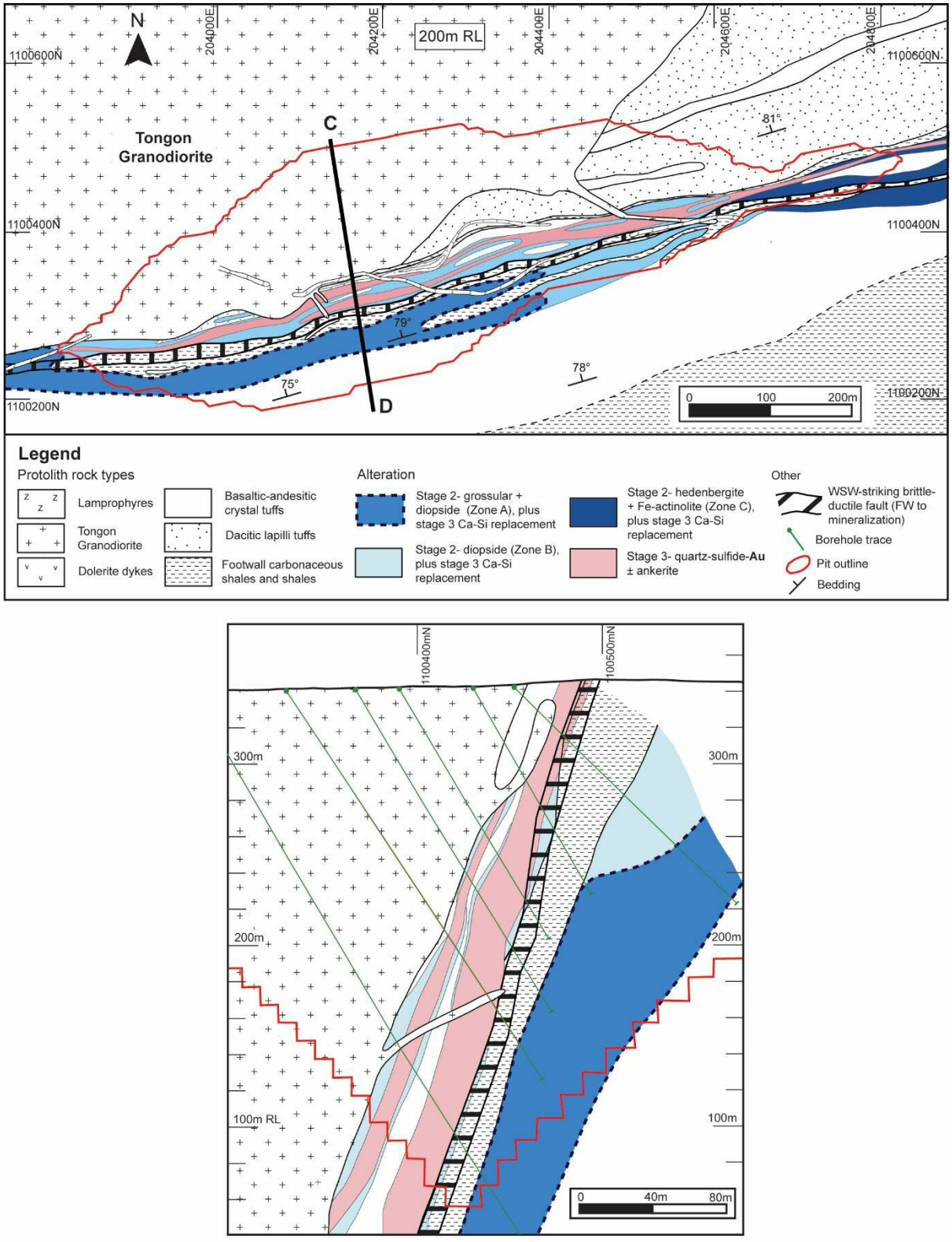

Figure 5 Typical flitch map (200 m R.L.) and cross section (C-D) of the Tongon North deposit, showing lithology, structure, and distribution of skarn. Only the western 1.2 km of the deposit is shown in the plan map. The extent of the stage 1 K alteration is not well constrained, although it is absent from the footwall shales and carbonaceous shales. The minor phase of late (stage 4) chlorite-sericite alteration is not shown. Note the plan and section images are a different scale. Same abbreviations as Figure 2.

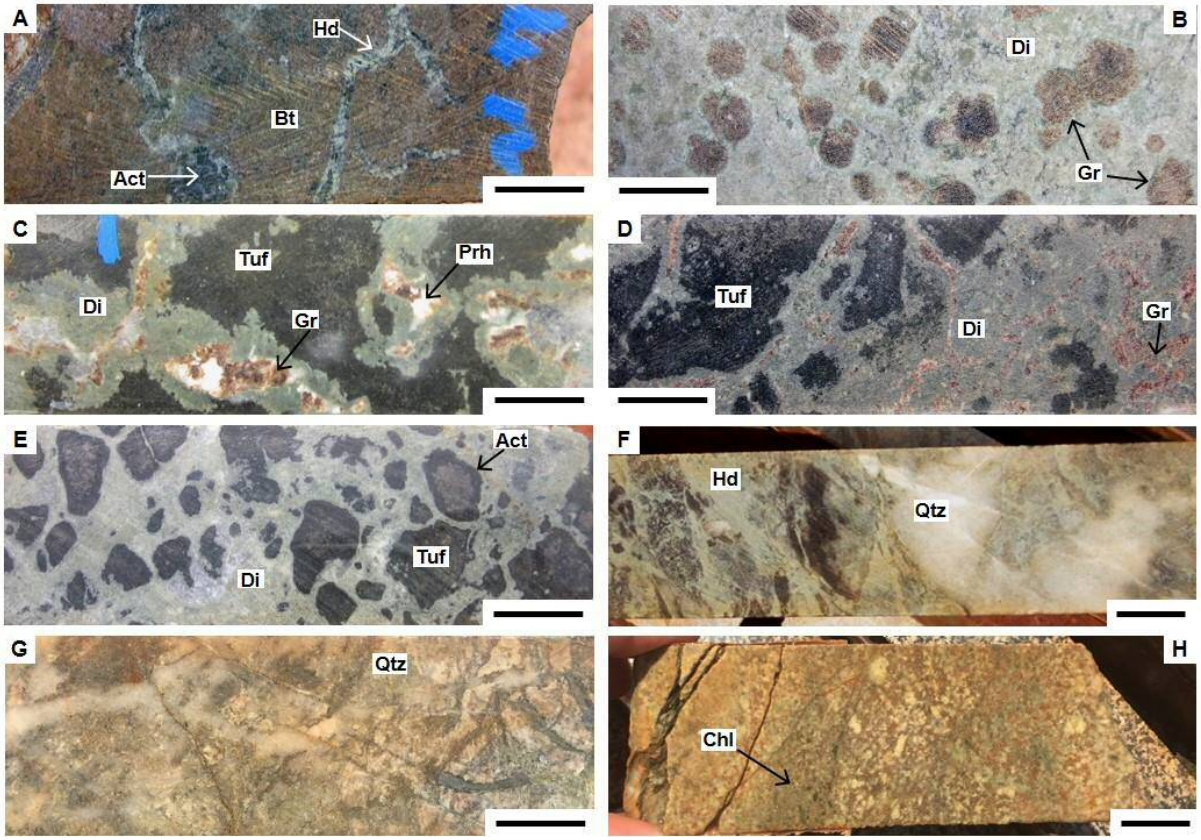

Figure 6 Drill core photographs showing the different alteration assemblages present in the Tongon host basaltic-andesitic tuffs and their relative timings. (A) Zone of strong, brown-colored, stage 1 biotite alteration with crosscutting stage 2 hedenbergiteactinolite veinlets. (B) Strong stage 2 diospide replacement of the host rocks with coarse (~1 cm) poikiloblastic grossular garnets. (C) Stage 2 grossular veins and veinlets overprinting fractured basaltic-andesitic tuff. Light green-gray diopside alteration selvages occur along the vein walls. Grossular is replaced by stage 3 prehnite and less common calcite (white phases). (D) Similar to (C) with wider diopside haloes surrounding grossular veinlets. (E) Pseudobreccia associated with stage 2 diopside replacement. Wall-rock clasts of unaltered basaltic-andesitic tuffs show pronounced actinolite reaction rims through replacement of primary hornblende. (F) Stage 3 patchy quartz alteration overprinting green stage 2 hedenbergite alteration. (G) Stage 3 multiphase quartz alteration associated with fine disseminated mineralized sulfides (arsenopyrite and pyrite). (H) Late chlorite-sericite (stage 4) alteration and deformation in the Tongon granodiorite. Unaltered example of this intrusive rock is shown in Figure 4G. Scale bar = 2 cm. Abbreviations: Act = actinolite, Bt = biotite, Chl = chlorite, Di = diopside, Gr = grossular garnet, Hd = hedenbergite, Prh = prehnite, Qtz = quartz, Tuf = unaltered basaltic-andesitic tuff.

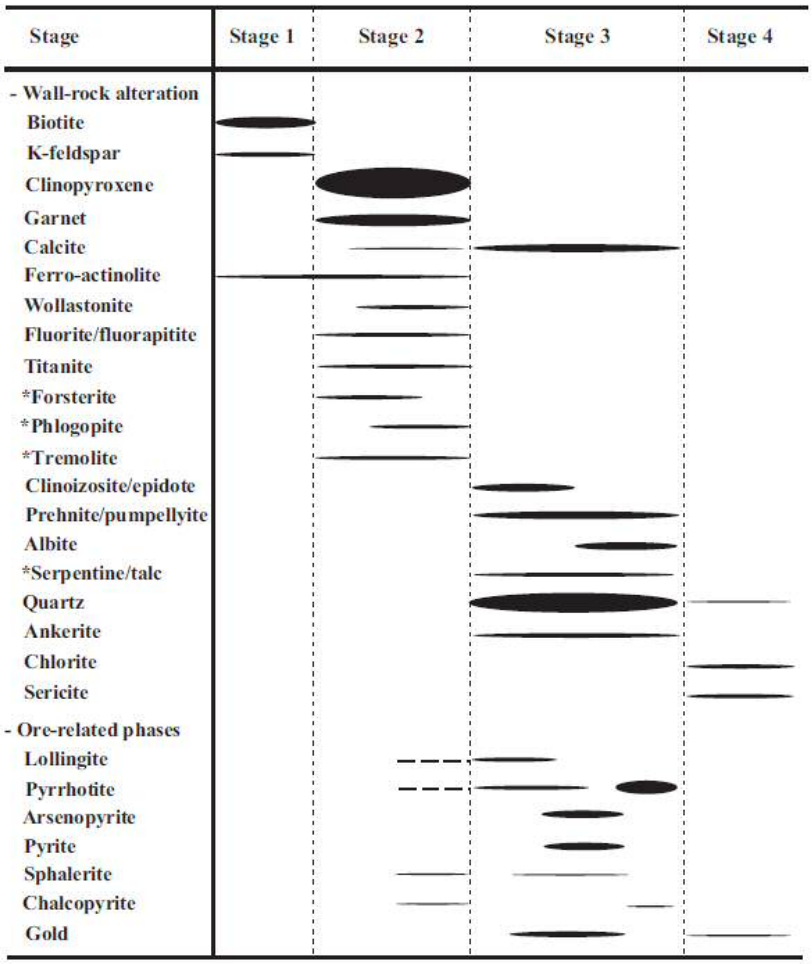

*Figure 7 Ore and alteration paragenetic sequence for Tongon (*refers to localized alteration).*

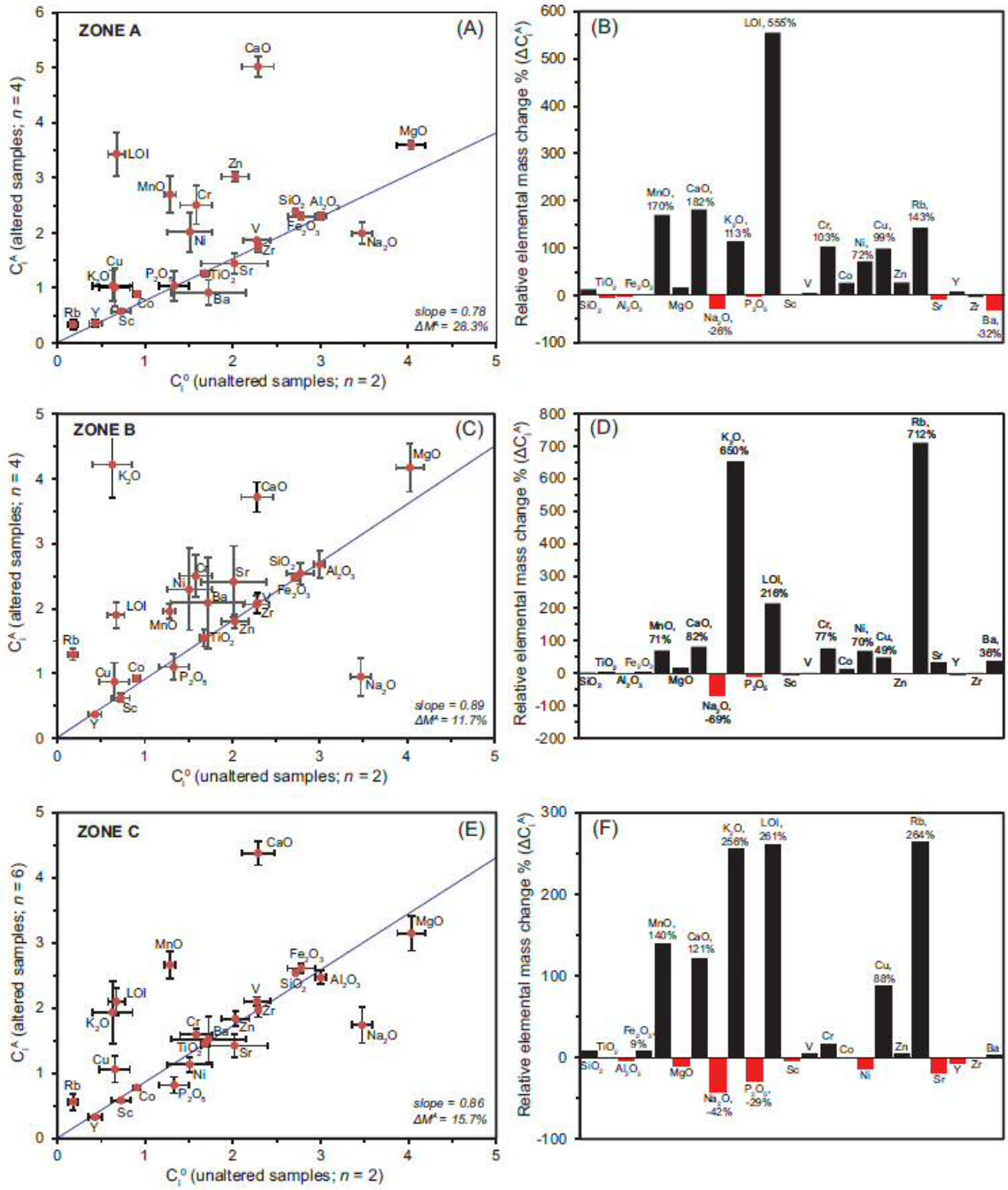

*Figure 8 Isocon diagrams (left) after Grant (1986) and mass-balance graphs (right) for skarn-altered samples at Tongon. Elements are displayed at different scales on the isocon plots to avoid stacking. The whole-rock geochemical data is shown in Table 1. (A-B) Zone A assemblages = biotite + K-feldspar stage 1), grossular + diopside (stage 2), plus calc-silicate retrograde replacement (stage 3). (C-D) Zone B assemblages = biotite + K-feldspar (stage 1), diopside (stage 2), plus calc-silicate retrograde replacement (stage 3). (E-F) Zone C assemblages = biotite + K-feldspar (stage 1), hedenbergite + actinolite (stage 2), plus calc-silicate retrograde replacement and weak quartz (stage 3). Strong stage 3 silicification (e.g., Fig. 6G) in zones B and C was not sampled for whole-rock geochemistry. Ci*O *and* Ci*A = initial (unaltered) and final (altered) concentrations in component* i*, respectively; DM*A *= net mass change during alteration; DC*i*A = mass changes for component* i*. Slope = slope of best-fit isocon defined by least-squared regression using immobile elements TiO2, Al2O3, Sc, Y, and Zr. Error bars = 1 standard error.*

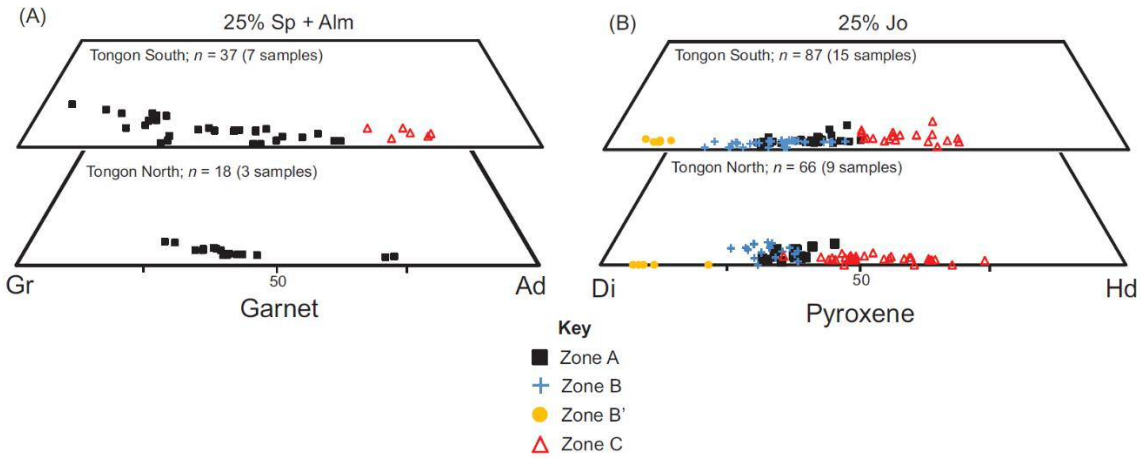

Figure 9 Composition of garnet (A) and pyroxene (B) at Tongon South and Tongon North. Garnet: grossular (Gr)-andradite (Ad)-spessartine (Sp)-almandine (Alm) solid solution; pyroxene: diopside (Di)-hedenbergite (Hd)- johannsenite (Jo) solid solution. Zone A = diopside + grossular; zone 2 = diopside; zone B = localized diopside + phlogopite + tremolite + forsterite; zone C = hedenbergite + ferro-actinolite + minor andradite. Data presented in Table A1.

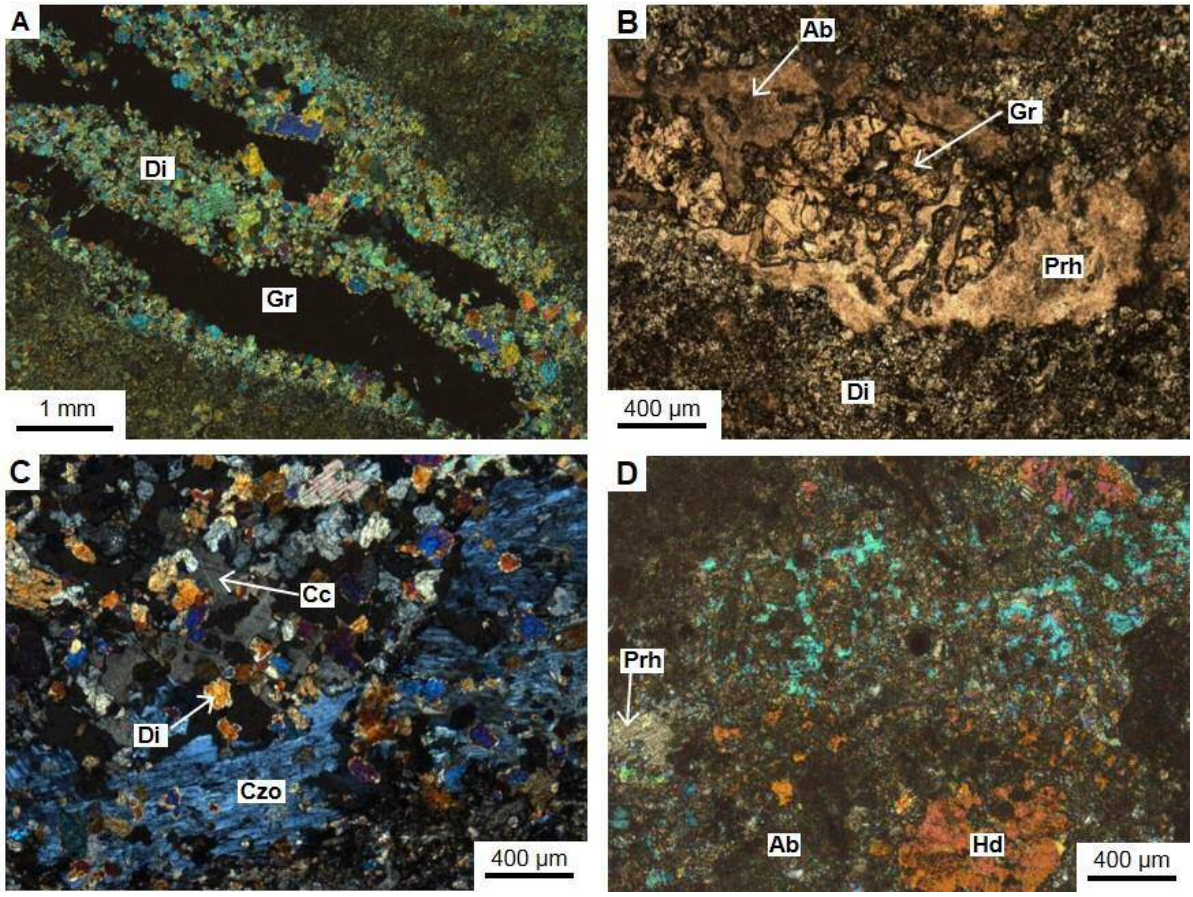

Figure 10 Photomicrographs showing the variable degrees of replacement of garnet and clinopyroxene by stage 3 calc-silicatecarbonate alteration assemblages. (A) Laminated pyroxene-garnet vein crosscutting basaltic andesitic tuff. Pyroxene-garnet vein shows only limited replacement by stage 3 calc-silicate-carbonate phases (XPL image). (B) Photomicrograph of Figure 6C showing aggregate of grossular garnet (yellow, high-relief grain in center of image) marginally replaced by prehnite and albite (PPL image). (C) Clinozoisite (blue interference colors) and calcite replacing fine-grained pyroxene (XPL image). (D) Zone C hedenbergite showing strong replacement by very fine grained amorphous albite and prehnite (XPL image). Abbreviations: Ab = albite, Cc = calcite, Czo = clinozoisite, Di = diopside, Hd = hedenbergite, Gr = grossular, PPL = planepolarized light, Prh = prehnite, XPL = cross-polarized light.

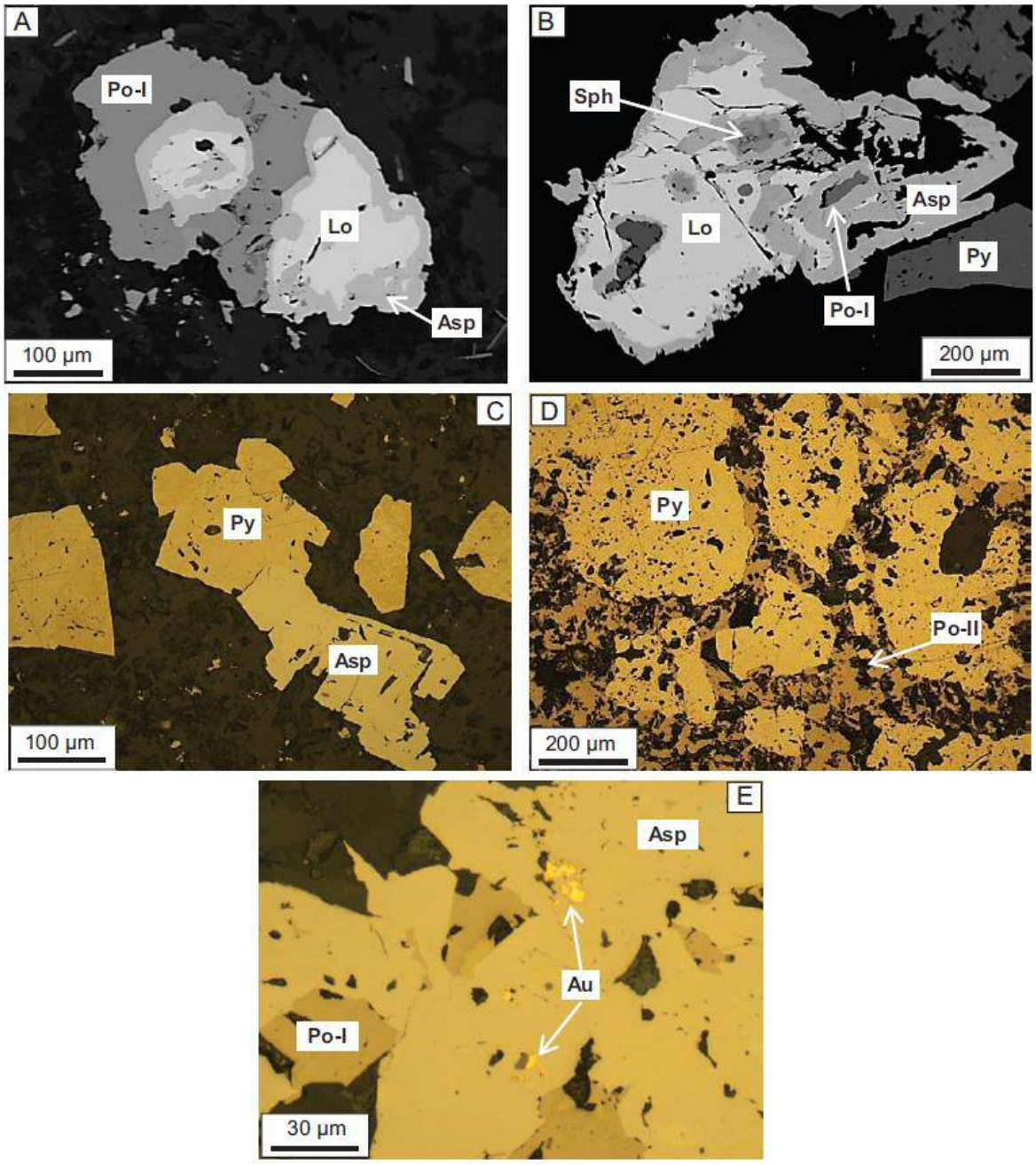

Figure 11 Back-scattered electron (A-B) and reflected light images (C-D) showing the sulfide paragenesis at Tongon. (A-B) Löllingite and pyrrhotite reacting to form arsenopyrite. (C) Arsenopyrite intergrown with pyrite. (D) Late pyrrhotite filling fractures in pyrite. (E) Cluster of gold inclusions in arsenopyrite. Abbreviations: Asp = arsenopyrite, Lo = löllingite, Po = pyrrhotite, Py = pyrite, Sph = sphalerite.

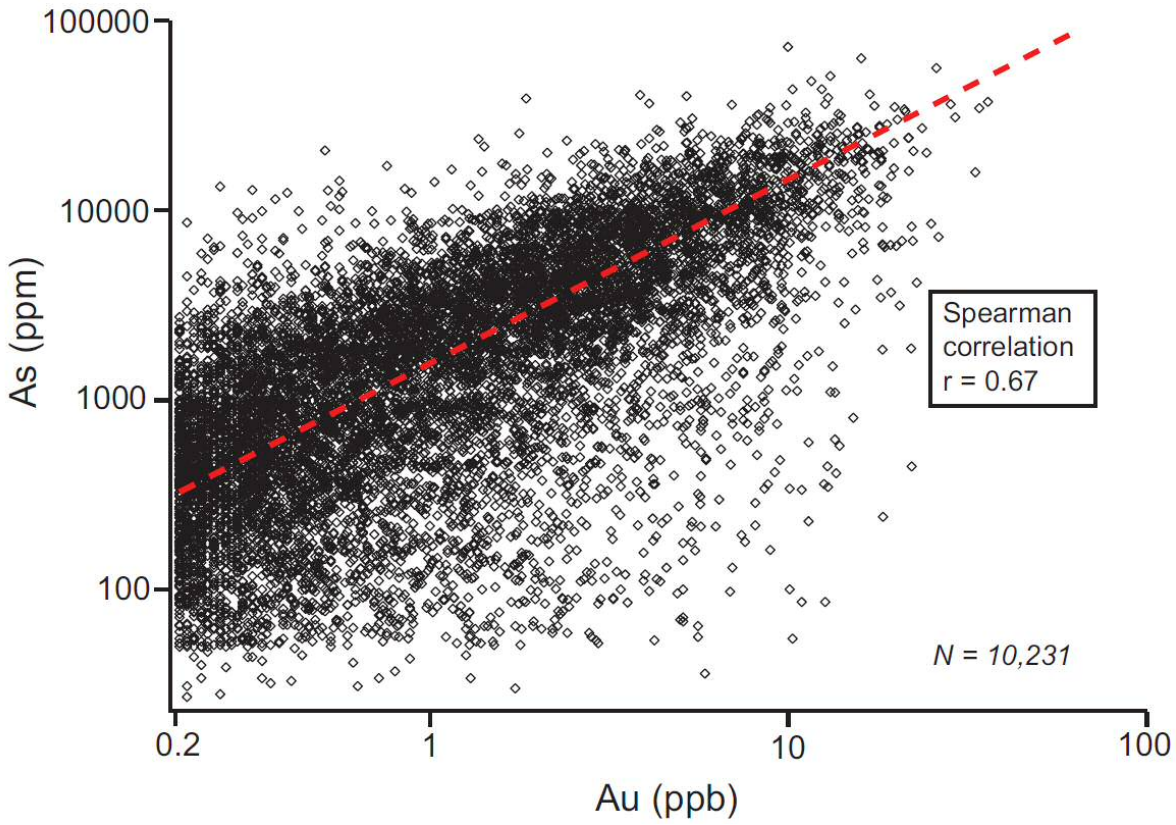

Figure 12 Bivariate plot showing Au-As correlation at Tongon South and Tongon North (data obtained from Allibone, 2013).

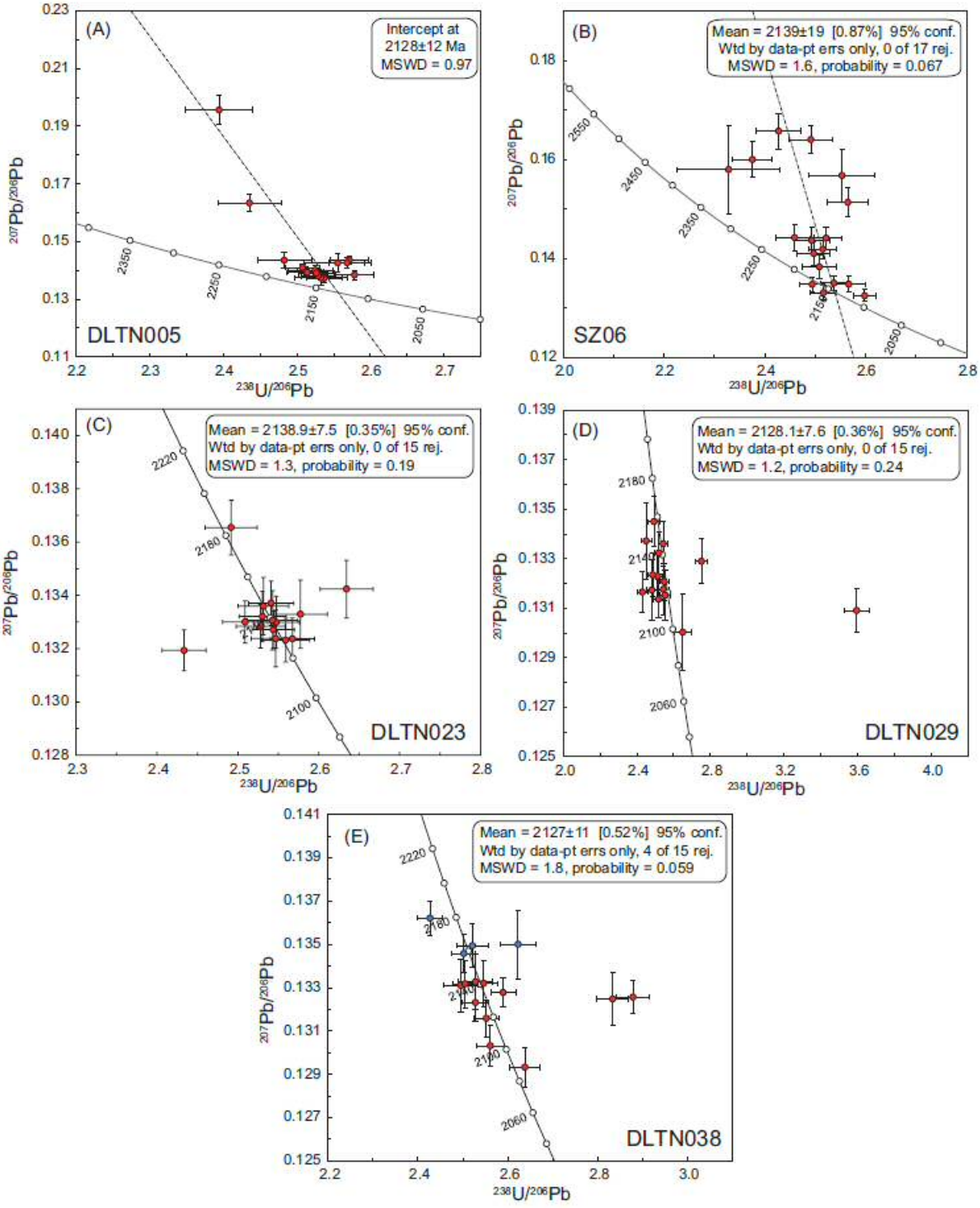

Figure 13 Tera-Wasserburg concordia plots of U-Pb isotopic composition of hydrothermal titanites (A-B) and magmatic zircons (C-E). (A-B) Stage 2 calc-silicate alteration from Tongon South (DLTN005 and SZ06). (C-E) Samples from the Tongon granodiorite (DLTN023 and DLT029 from Tongon South; DLTN038 from Tongon North). All ages are calculated as weighted averages of Pb^{207}/Pb^{206} ages, except DLTN005 (A), which was calculated from the concordia intercept. Zircon grains indicated by red circles were used for age calculation, whereas those indicated by blue circles were discarded. Error bars are 1 standard error.

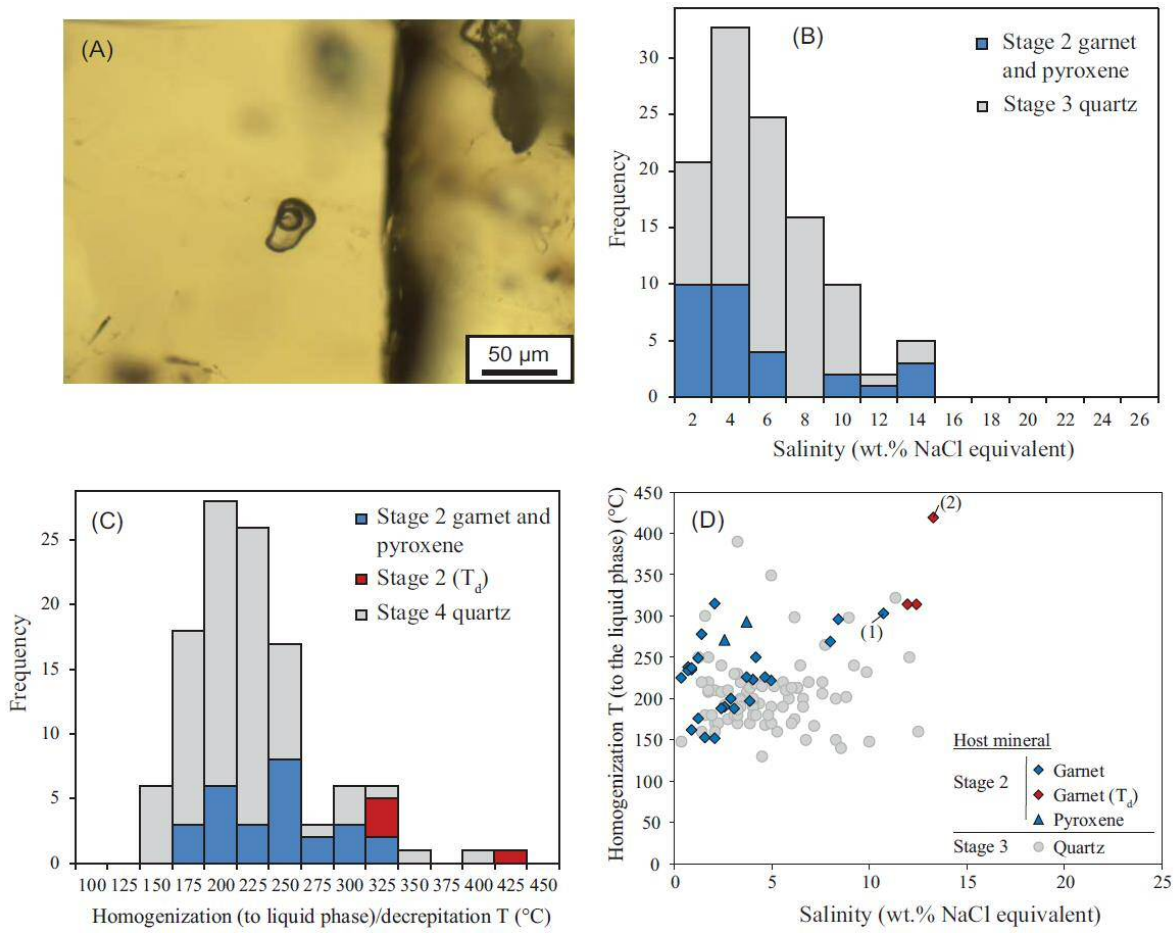

Figure 14 Fluid inclusion data collected from Tongon South and Tongon North stage 2 and stage 3 alteration zones (A) Photomicrograph of a high T aqueous fluid inclusion in the core of stage 2 garnet crystal (inclusion decrepitated at 365°C). (B) Histogram showing the salinity ranges calculated from ice melting temperatures, using the Zhang and Frantz (1987) equation of state. (C) Histogram showing the spread of homogenization temperatures (to the liquid phase). (D) Salinity vs. homogenization temperature scatter plot. Td = inclusions that decrepitated prior to final homogenization.

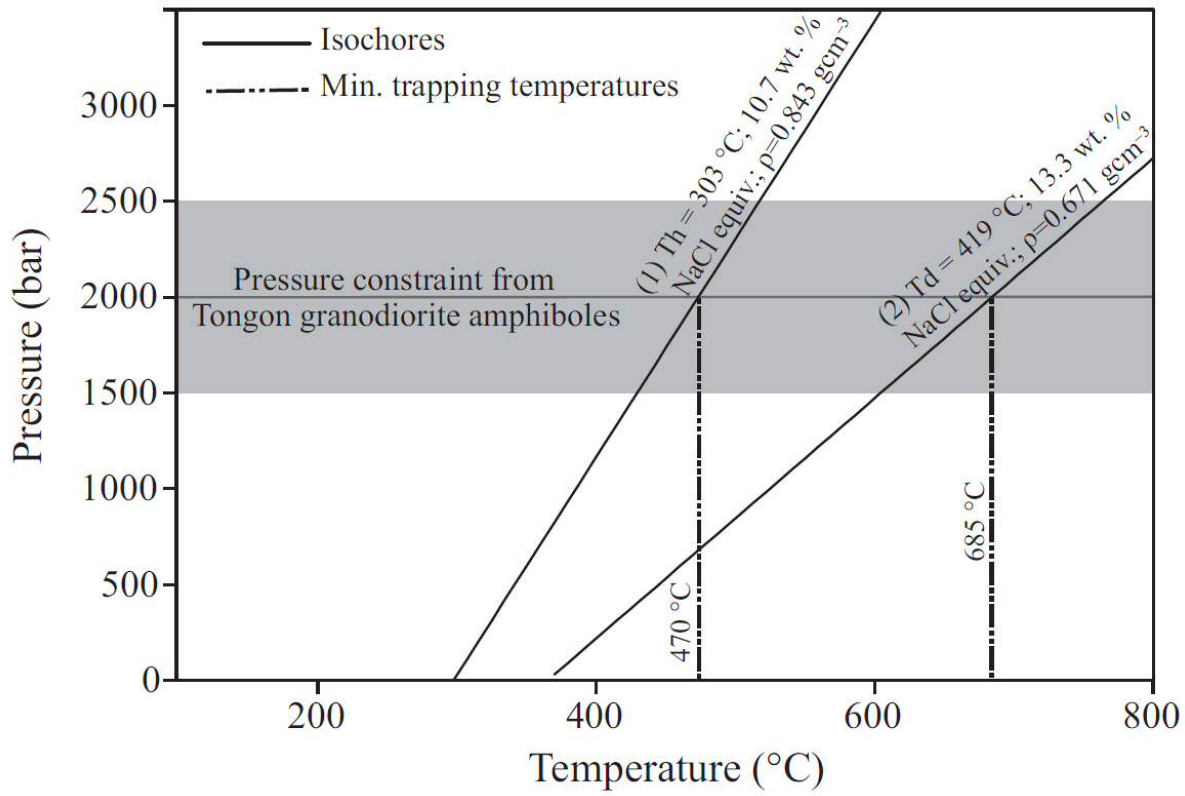

Figure 15 Pressure-temperature plot showing minimum and maximum isochores for primary H_2O-salt inclusions in prograde garnet samples at Tongon (inclusions 1 and 2 on Fig. 14D). Pressure is constrained using the Al in amphibole geobarometer of Hammarstrom and Zen (1986) applied to hornblende in the Tongon granodiorite (Table A1), gray field indicates error (± 0.5 kbar). Vertical dashed lines represent pressure-corrected minimum trapping temperatures. Bulk fluid properties are stated with the corresponding isochores and were calculated using the FLUIDS software of Bakker (2003).

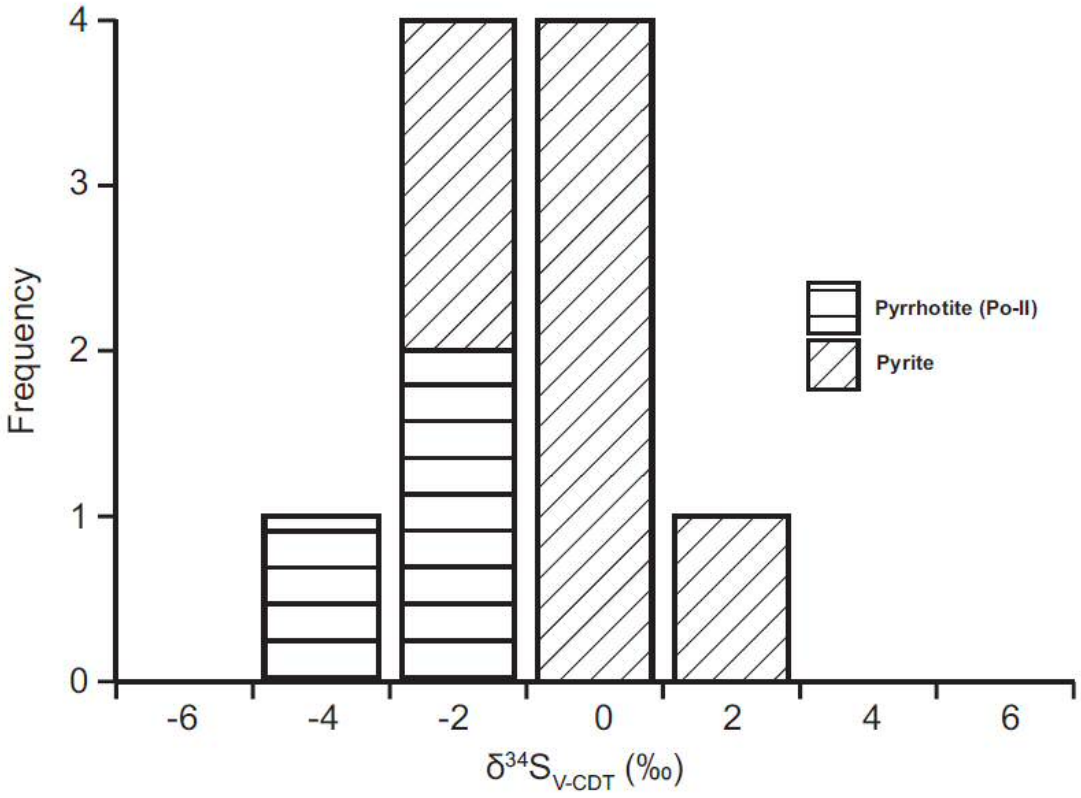

Figure 16 Histogram of the $\delta^{34}S$ data collected from stage 3 sulfides.

Table 1 Whole-Rock Geochemical Data Collected from Selected Unaltered and Altered Samples at Tongon. Note: Moderate to strong silica-altered (stage 3) samples not included in this dataset.

	Unaltered rocks						Skarn-altered basaltic-andesitic tuffs													
	Tongon granodiorite				Basaltic-andesitic tuffs		Zone A				Zone B				Zone C					
Sample ID	DLTN 023	DLTN 024	DLTN 029	DLTN 038	DLTN 071	SZ13	DLTN 005	DLTN 006	DLTN 025	DLTN 067	DLTN 003	DLTN 066	DLTN 072	SZ06	DLTN 008	DLTN 016	DLTN 026	DLTN 065	DLTN 021	SZ07
SiO_2	67.04	67.9	67.75	67.28	54.58	53.95	49.89	49.02	46.66	45.67	50.65	50.31	47.05	50.3	48.92	52.78	49.92	51.39	49.88	52.32
TiO_2	0.47	0.44	0.44	0.42	0.86	0.81	0.71	0.64	0.61	0.58	0.77	0.65	0.72	0.96	0.66	0.82	0.71	0.63	0.78	0.73
Al_2O_3	14.09	14.23	14.37	14.27	12.26	11.76	9.11	8.81	9.83	9.15	12.22	8.33	10.27	11.16	11.28	10.08	10.01	10.02	9.78	8.33
Fe_2O_3T	4.49	4.04	4.07	4.26	10.49	11.74	8.96	9.65	9.63	8.53	10.09	10.51	11.58	8.47	11.08	11.5	9.74	9.1	10.73	10
MnO	0.07	0.07	0.06	0.07	0.13	0.12	0.24	0.36	0.21	0.28	0.19	0.17	0.21	0.22	0.26	0.18	0.28	0.26	0.26	0.29
MgO	2.98	2.67	2.81	2.97	7.75	8.38	6.88	7.19	7.63	7.05	6.98	10.02	9.16	7.22	6.58	4.06	5.87	5.3	7.00	7.25
CaO	4.25	3.76	3.96	3.37	9.87	8.41	18.67	19.64	19.81	22.18	12.31	14.97	16.70	15.5	16.22	16.65	18.87	17.68	17.21	15.48
Na_2O	4.04	4.06	4.08	4.04	3.59	3.35	2.48	1.95	1.52	2.01	1.62	1.06	0.20	0.93	2.13	2.1	1.79	2.48	2.75	1.98
K_2O	2.06	2.4	2.43	2.04	0.21	0.43	0.41	0.49	0.91	0.27	2.38	1.42	2.05	2.59	0.75	0.3	0.91	0.81	0.32	1.92
P_2O_5	0.21	0.18	0.18	0.19	0.23	0.3	0.13	0.21	0.36	0.13	0.2	0.17	0.18	0.33	0.24	0.15	0.19	0.19	0.24	0.15
LOI	0.9	1.54	1.05	1.75	0.77	0.58	2.79	2.72	4.05	4.18	1.97	1.41	2.39	1.83	2.27	1.38	2.88	3.19	2.10	1.72
Total	100.59	101.3	101.21	100.66	100.75	99.83	100.26	100.68	101.22	100.02	99.38	99.02	100.49	99.5	100.38	99.98	101.17	101.04	101.06	100.17
Sc (ppm)	9.8	8.9	8.9	8.8	31	41.4	27.7	24.2	31.49	31.9	30.7	22.00	37.37	34.5	32.1	31	28.7	19.6	25.84	24.7
V	67.8	63.1	60.2	68.7	242.5	212.3	184	189.9	186.39	186.2	234.5	171.15	211.61	209	227.1	229.6	192	167.8	217.23	191.3
Cr	105.6	82.3	95.7	113.3	176.7	139.7	317.8	301.3	175.45	208	192.8	205.31	268.87	334.2	128.5	178.9	156.9	131.3	187.16	178.6
Co	13.7	12.5	12.2	13.9	43.2	47.3	51.7	41.5	40.33	45.1	46.6	49.39	47.13	41.2	39.4	39.6	38.2	31.9	43.68	39.5
Ni	63.8	110	78	63.8	62.6	88.2	142.3	118.2	63.20	79.5	80.6	83.32	85.82	209.4	50.1	62.8	52.6	54.1	66.57	79
Cu	60.2	36.3	74.9	14.6	48	82.6	39.9	103.6	197.30	63.9	171.3	61.08	80.85	35.9	130.5	75.2	100	30.9	81.01	182.9
Zn	54.8	53.7	69.6	47.8	109.3	93.6	96.7	108.1	108.00	90.2	79.5	97.48	100.74	83.3	88.4	117.7	87.9	92.2	90.90	87.9
Ga	17.7	17.5	17.1	18.5	15.1	14.4	13.2	12.9	13.5	11.6	19.9	12.3	14	12.3	15.8	13.4	14.8	16.7	14.9	13.4
Rb	48.9	59.5	54.7	57.8	6.3	11.5	14.4	17	28.43	7.5	67.5	51.65	67.60	71.4	21.9	8.4	31.5	23.2	10.20	50.4
Sr	171.1	151.3	151.3	165.5	478.5	327.7	235.3	338.3	212.09	370.6	650.8	261.52	328.23	690	291.7	346.7	373.8	455.2	358.87	148.2
Y	11.3	11.7	11.9	12.5	17.8	19	13.4	16	17.77	15.4	18.8	17.01	18.88	19.5	20.3	16.3	15.9	12.9	17.63	14.1
Zr	142.1	132.6	139.6	154.5	75.4	77.1	60.5	61.4	58.85	49.9	61.1	82.02	60.97	73.7	75.2	56.9	72.8	78	78.24	67.3
Nb	4.38	4.87	4.12	5.6	3.26	3.54	2.81	2.66	2.37	1.83	4.37	2.74	2.52	3.88	3.59	2.55	3.06	3.17	3.29	2.95
Mo	0.52	0.6	0.49	0.6	0.18	0.42	0.91	1.02	1.39	7.53	0.12	0.19	0.12	0.24	0.69	0.11	0.37	0.58	0.14	0.81
Sn	2.43	3.1	3.66	2.91	1.75	2.87	1.28	1.85	0.97	8.86	1.38	1.90	1.58	1.25	1.56	2.79	1.56	1.78	1.08	1.3
Cs	1.43	1.67	1.04	2.4	0.53	0.6	0.83	0.7	1.14	0.33	4.01	2.48	5.78	1.74	1.62	0.34	1.43	1.24	0.51	0.64
Ba	856	755.4	714.3	738.6	258.8	429.6	153.2	321.1	117.09	141.7	549.6	138.10	239.01	745.5	219.3	115	553.5	318.4	100.7	371.3
La	37.48	32.93	32.81	34.74	10.2	12.46	8.86	9.29	5.99	3.95	14.24	8.89	6.10	10.84	10.25	6.88	9.35	8.27	9.03	8.51
Ce	73.49	66.74	61.48	70.26	24.17	30.88	20.86	20.74	13.91	9.64	34.04	19.82	14.14	27.99	23.17	16.27	20.02	18.56	20.90	16.9
Pr	8.41	7.79	6.84	8.29	3.53	4.58	3.03	3.00	2.14	1.43	4.96	2.84	2.15	4.21	3.3	2.44	2.8	2.66	3.04	2.51
Nd	28.14	26.28	22.55	28.19	14.73	20.28	13.11	12.97	9.45	6.73	20.18	11.71	9.63	18.56	14.21	10.77	11.96	11.27	13.07	10.63
Sm	4.72	4.77	3.75	5.04	3.34	4.79	3.08	2.96	2.61	1.7	4.27	2.66	2.57	4.2	3.57	2.75	2.81	2.53	3.13	2.44
Eu	1.22	1.14	1.08	1.21	1.07	1.34	0.88	0.93	0.96	0.62	1.27	0.90	0.86	1.35	1.22	0.86	0.92	0.91	0.96	0.75
Gd	3.52	3.32	2.83	3.61	3.52	5.1	2.76	2.91	3.16	2.09	3.93	2.34	2.84	4.02	3.43	2.78	2.81	2.44	3.12	2.53
Tb	0.41	0.41	0.34	0.44	0.55	0.83	0.43	0.47	0.58	0.35	0.62	0.39	0.47	0.6	0.58	0.48	0.46	0.37	0.49	0.39
Dy	1.9	1.82	1.57	1.93	3.36	5.04	2.43	2.79	3.89	2.44	3.33	2.29	3.08	3.45	3.6	2.99	2.61	2.25	3.15	2.32
Ho	0.33	0.32	0.28	0.35	0.61	0.94	0.45	0.51	0.85	0.46	0.6	0.42	0.56	0.65	0.69	0.57	0.51	0.44	0.59	0.44
Er	0.91	0.92	0.76	0.98	1.86	2.77	1.3	1.5	2.71	1.5	1.77	1.20	1.78	1.77	2.01	1.57	1.48	1.32	1.66	1.32
Tm	0.15	0.15	0.12	0.15	0.25	0.45	0.19	0.2	0.44	0.23	0.28	0.19	0.29	0.26	0.31	0.24	0.23	0.19	0.26	0.2
Yb	0.9	0.9	0.78	0.99	1.7	2.76	1.22	1.38	2.93	1.48	1.77	1.29	1.78	1.68	1.95	1.54	1.44	1.33	1.58	1.27
Lu	0.15	0.14	0.14	0.16	0.29	0.47	0.21	0.23	0.51	0.25	0.3	0.21	0.29	0.27	0.33	0.25	0.25	0.23	0.26	0.22
Hf	3.41	3.19	3.3	3.68	1.91	1.91	1.42	1.48	1.35	1.07	2.17	1.83	1.38	2.05	1.8	1.3	1.68	1.87	1.90	1.56
Ta	0.3	0.42	0.26	0.44	0.2	0.23	0.15	0.14	0.12	0.11	0.25	0.17	0.15	0.21	0.21	0.18	0.18	0.17	0.21	0.15
Pb	8.13	6.99	8.81	7.93	2.35	2.05	4.34	3.08	1.99	4.98	3.04	2.67	1.81	1.54	2.13	3.64	1.6	1.82	2.59	1.08
Th	5.48	6.46	5.1	6.72	0.79	0.82	0.79	0.58	0.40	0.29	1.08	1.05	0.34	0.86	0.84	0.79	0.58	0.65	0.69	0.65
U	1.7	2.6	1.73	2.55	0.52	0.78	0.31	0.44	0.38	0.35	0.86	0.31	0.33	0.59	0.44	0.33	0.36	0.53	0.70	0.3
Ti/Y	249.3	225.4	221.6	201.4	289.6	255.5	317.6	239.7	206.7	225.7	245.5	229.9	229.0	295.1	194.9	301.5	267.6	292.7	266.1	310.3

Table 2 Summary of Skarn Mineral Zonation at Tongon. [1]Refers to localized alteration assemblages.

Zone	Main stage 2 alteration phases	Stage 3 replacement phases	Skarn color and relative grain size
Zone A	Grossular + diopside	Epidote + clinozoisite + calcite + prehnite + actinolite + albite	Pale to light green, Fine- to coarse-grained
Zone B	Diopside	Epidote + prehnite + calcite + albite + pumpellyite	Light green, fine- to moderate-grained
	[1]Diopside + tremolite + forsterite + phlogopite	[1]Talc + serpentine + calcite + magnetite + anhydrite	Pale, fine-grained
Zone C	Hedenbergite + ferro-actinolite + wollastonite ± minor local andradite	Pumpellyite + prehnite + albite + calcite	Light to dark green, fine-grained